J. Fluid Mech. (1998), *vol.* 376, *pp.* 1–35. Printed in the United Kingdom

© 1998 Cambridge University Press

Vortex dynamics in a spatially accelerating shear layer

By G. PAWLAK† AND L. ARMI

Applied Mechanics and Engineering Sciences and Scripps Institution of Oceanography, University of California San Diego, La Jolla, CA, 92093-0230, USA

(Received 7 October 1997 and in revised form 27 May 1998)

An experimental and analytical study into the vortex dynamics of a stratified shear layer subjected to a spatial acceleration is presented. The outer flow is dictated by a hydraulically controlled wedge flow which provides a spatially accelerating shear layer and baroclinic generation of vorticity along the inclined interface. A new, finite-amplitude mechanism is observed in which the core of the growing vortex is separated from the vorticity source at the interface. A secondary core develops and an altered vortex pairing interaction is observed. A spatial linear stability analysis reveals that one of two modified Kelvin–Helmholtz modes is dominant, resulting in the centre of the instability being offset from the density interface into the slower moving stream. Digital particle imaging velocimetry (DPIV) measurements are presented along with flow visualization which indicate that the mechanism is a result of the offset in the vortex core from the source of vorticity at the interface combined with the effects of spatial acceleration and buoyancy. The mixing induced by the interfacial instabilities is such that a sharp density interface remains near the high-momentum stream, with a low-gradient region extending into the low-momentum stream.

1. Introduction

Specific problems involving shear-induced mixing in geophysical applications often occur in complex scenarios in which both stratification and geometric boundary conditions may have significant effects on mixing layer dynamics. One effect of geometrical boundary conditions on a stratified mixing layer is an acceleration due to internal hydraulic response to topographical changes.

A number of geophysical flows can be described in terms of internal hydraulics. The review by Smith (1979) examines atmospheric hydraulic response to mountain topography. Klemp & Lilly (1975) used hydraulic modelling to describe large-scale atmospheric flows responsible for severe downslope wind events. Flow in ocean straits, such as the Strait of Gibraltar, has also been considered within the context of internal hydraulics (Armi & Farmer 1988). An important scenario in which hydraulic flow and interfacial mixing processes are inextricably linked is that of estuarine flow. Farmer & Freeland (1983) present a general study of fjord systems and identify mixing mechanisms as central to circulation in estuaries, since these mechanisms are responsible for establishing the density gradients that drive the gravitational flow.

Geyer & Smith (1987) studied an estuarine system in Fraser Estuary in British Columbia in which a number of localized mixing zones could be identified, coincident with lateral constrictions in the channel. In addition to the baroclinic circulation,

† Present address: School of Oceanography, University of Washington, Seattle, WA 98107, USA.

https://doi.org/10.1017/S002211209800250X Published online by Cambridge University Press

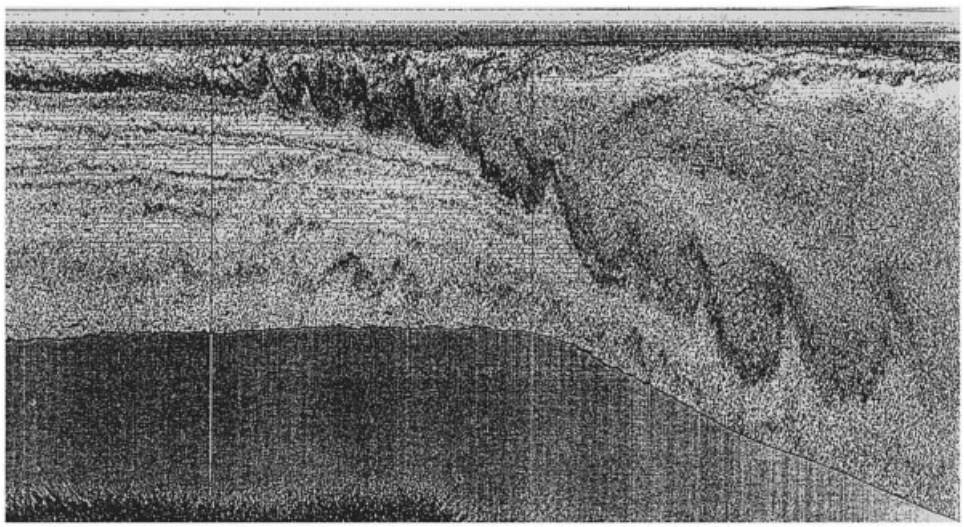


FIGURE 1. Echosounder image of plunging flow at Knight Inlet, British Columbia. Tidal flow is from left to right. Channel depth at the right of the image is approximately 60 m. The horizontal scale is approximately 0.5 km (personal communication, D. Farmer).

estuaries are subject to strong tidal forcing. The baroclinic exchange may be arrested in the presence of strong tidal flow, resulting in tidal intrusions or salt wedge flows. These flows have been observed and studied extensively in Knight Inlet in British Columbia by Farmer & Smith (1980) and Farmer & Armi (1998). Figure 1 is an echosounder image (D. Farmer, personal communication) of flow over a sill in Knight Inlet showing a plunging interface, which can be identified with a strong density step from concurrent density measurements. The image was obtained with a 100 to 200 KHz echosounder from a ship traversing the flow region. Reflections from waterborne scatterers (presumably biological) serve as markers which reveal flow structure when the reflected signal is plotted versus depth. Tidal flow is seaward, from left to right, with the fluid below the plunge line being composed of dense salt water trapped by earlier tidal cycles. A thin layer of fresh water from glacial runoff caps the flow. The dense fluid flows over the sill, plunges near the crest and accelerates as it descends. Since the time for the ship to traverse the region is finite, there is some spatial aliasing of the image. Nonetheless, qualitative observations of flow structure are possible. Large-scale shear instabilities are visible along the plunge line. The region above the shear interface is essentially homogeneous, composed of mixed fluid locally generated along the plunge line (Farmer & Armi 1998). The details of the general flow are thus determined by the interfacial mixing.

1.1. *Two-layer hydraulic theory*

Flow in these inlets is quite often characterized by high stratification and can be modelled using hydraulic theory for two homogeneous layers. The hydraulic theory for the flow of two fluids of differing densities through variations in geometry is detailed in Armi (1986). The special case of two counter-flowing layers in a contraction is considered by Armi & Farmer (1986). These exchange flows are characterized by the existence of two control locations, at which the flow is critical to long internal waves. A sketch of the exchange flow is shown in figure 2(*a*). One control coincides with the narrowest section of the channel (b_0) and the second location, a 'virtual control', occurs at the point at which layer velocities are equal (b_v). Flows are parameterized in

https://doi.org/10.1017/S002211209800250X Published online by Cambridge University Press

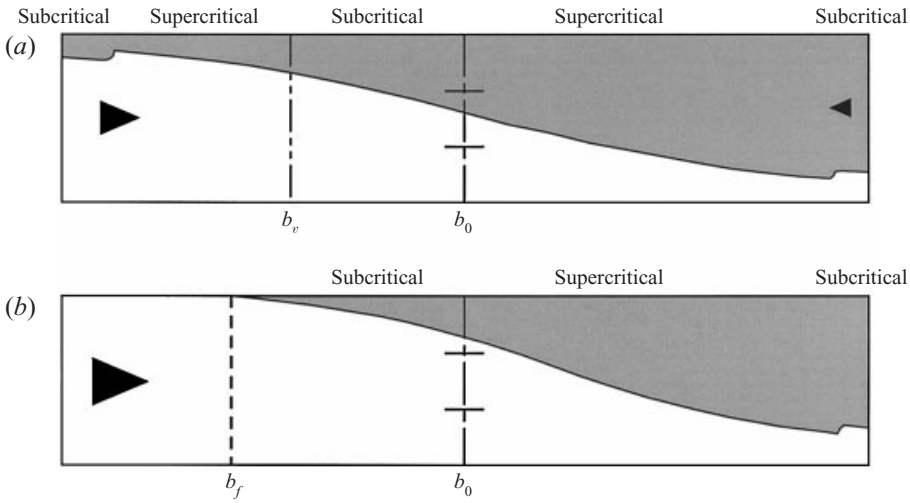


FIGURE 2. Regimes of two-layer hydraulic flow. Triangles indicate direction and relative scale of flow. (*a*) Weak to moderate barotropic exchange flow; b_0 indicates the narrowest section and b_v is the location of the virtual control. (*b*) Arrested wedge flow occurring for moderate to strong barotropic component; b_f indicates the position of the tip of the wedge.

terms of the net barotropic flow rate, with distinct flow regimes occurring for 'weak', 'moderate' and 'strong' barotropic flow. For the case of zero net flow rate, both layers have equal and opposite flow rates and both control conditions are satisfied at the narrowest point of the channel. Flow is supercritical on either side of this point, matching the subcritical conditions in the reservoirs through hydraulic jumps. The introduction of a weak net flow results in shifting of the virtual control towards the upstream reservoir, with subcritical conditions existing between the controls and supercritical flow occurring elsewhere.

Wedge flows are a special case of two-layer exchange flows, occurring in the limit of moderate and high barotropic flow. These flows, illustrated in figure 2(*b*), result for barotropic flow rates exceeding a critical value, at which the virtual control condition is satisfied in the upstream reservoir. At this critical point, one layer is arrested and the flow is effectively a single layer flow. For moderate barotropic flow rates, the wedge tip (b_f) is located upstream of the channel narrows and the flow is subcritical to long waves, accelerating through a single control at the narrowest section to supercritical conditions downstream. For high flow rates, the wedge tip occurs downstream of the narrowest section at which point the control condition is met. The moderate and high barotropic flow regimes are considered in detail by Pawlak & Armi (1997), including the effects of friction and cross-stream non-uniformity.

1.2. *Mixing layer and stability studies*

As evidenced in figure 1, the interface between the two layers is subject to shear instabilities which can generate significant mixing. These instabilities are spatially evolving and are subject to spatially varying velocity fields.

Experimental studies of mixing layers have typically been undertaken in spatially evolving splitter-plate configurations (Brown & Roshko 1974; Winant & Browand 1974) or in temporally evolving tilting tube facilities as described by Thorpe (1968). These investigations have documented the existence of organized two-dimensional vortical structures in the mixing layer and identified the interaction of these structures as a key component in the growth of the mixing layer. Subsequent studies have given

https://doi.org/10.1017/S002211209800250X Published online by Cambridge University Press

valuable insight into mixing layer mechanics such as the source of streamwise vorticity (Thorpe 1985; Lasheras, Cho & Maxworthy 1986; Bernal & Roshko 1986) and its role in the mixing transition. Experimental studies by Koop & Browand (1979) and Thorpe (1971, 1973) have also aided in understanding the effects of stratification on the mixing layer.

The development of the unstratified, non-accelerating shear layer involves essentially a redistribution of a finite amount of vorticity by large-scale two-dimensional structures (Corcos & Sherman 1984). Stratification can provide both a source and a sink for vorticity. For the non-accelerating, stratified case (Koop & Browand 1979), baroclinicity affects the redistribution of the initial vorticity and ultimately limits the rate of growth of the mixing layer.

The stratified layer subjected to a temporal acceleration was examined by Thorpe (1968, 1971) in his well-known tilting tube experiments. Unstratified spatially accelerating shear layers have been considered within the context of confined reacting shear layers, in which a pressure gradient is generated by the heat release from the reaction. Hermanson & Dimotakis (1989) examined the thinning of a reacting shear layer in the presence of a favourable pressure gradient and parameterized the rate of growth of the mixing layer as an integral of the varying velocity ratio.

The stability of two-layer exchange flows to long internal waves was examined by Lawrence (1990). He found that these flows become unstable to infinitely long waves downstream of the narrowest section in the presence of a net barotropic flow. Pawlak & Armi (1996) considered the stability of exchange flows using temporal linear stability theory and found various possible modes of instabilities for different flow regimes.

Analysis of the linear stability of inviscid flows to infinitesimal perturbations has been used in obtaining a qualitative description of shear instabilities in a number of studies. The majority of analyses of shear instabilities have been conducted from a temporal frame of reference. The classical analyses by Taylor (1931) and Goldstein (1931) yielded the equation governing the evolution of infinitesimal disturbances and examined the temporal solution space for basic profiles. Holmboe (1962) investigated the case in which the shear thickness is much larger than the density interface. An additional region of instability occurs at higher Richardson numbers for this case which he termed *overstability* and which has since become identified as the Holmboe instability.

Hazel (1972) considered the effects of equidistant boundaries on profiles with equal density and velocity scale and further detailed the effects of a variation in relative scales of the density and velocity interfaces. Lawrence, Browand & Redekopp (1987) followed by Lawrence, Lasheras & Browand (1991) found that an offset in the centres of the velocity and density interfaces resulted in the dominance of one of the two Holmboe modes. These temporal studies can be qualitatively extended to spatially developing flows and can be extrapolated in cases where the convective velocity is large in comparison to the mean shear. In the arrested wedge, however, this condition is not satisfied and the problem must be considered from a spatial frame of reference.

The spatial linear stability of the unstratified shear layer was addressed by Michalke (1965). Among other discrepancies, he found that the disturbance phase velocity was not constant with frequency as predicted by temporal theory. His spatial theory predictions agreed well with experimental observations in spatially developing shear layers.

1.3. *Purpose*

Several recent studies have used hydraulically controlled flows as a framework for the study of interfacial shear phenomena (Pawlak & Armi 1996; Yonemitsu *et al.* 1996)

https://doi.org/10.1017/S002211209800250X Published online by Cambridge University Press

without addressing the effects of acceleration. We shall examine the vortex mechanisms which are inherent in some of these hydraulic flows in which acceleration is significant on the scale of instability development.

The aim of the present study is to examine the combined effects of buoyancy and acceleration on the dynamics of a mixing layer. In § 1.4 we propose a parameter obtained from a time scale analysis of the relevant mechanisms. Section 2 presents a detailed description of the experimental facility and technique including laser-induced fluorescence (LIF) flow visualization and digital particle imaging velocimetry (DPIV). In § 3 we present experimental observations of the mixing layer mechanics for three experimental geometries. We will use spatial linear theory in § 4 to examine the possible modes of instability in the parallel flow case and to understand the effect of these modes on the accelerating mixing layer development. Experimental observations will be used along with the predictions from the stability analysis to generate a phenomenological description or cartoon of the development of these modes at finite amplitude in § 5. Consequences of the observed vortex mechanics on the mixing process will be quantified and discussed.

1.4. *Time scales*

We now seek a parameter that will serve as a measure of the local effect of the spatial acceleration on the developing mixed layer for various experimental geometries to be detailed in § 2. We will discuss the validity of this parameter choice further in § 5.

We can obtain a time scale for the vortex development using the vertical length scale of the mixed layer, δ, in combination with the overall shear, ΔU, or for a single flowing layer, U:

$$t_e = \frac{\delta}{U}. \tag{1.1}$$

This is, alternatively, the turnover time scale of the largest eddies. An acceleration time scale can be defined as

$$t_a = \left(\frac{c}{U} \frac{\mathrm{d}U}{\mathrm{d}x} \right)^{-1} \tag{1.2}$$

in which U is the free-stream velocity and c is the propagation velocity of the instability. This time scale is, in turn, equivalent to the time over which a parcel of fluid travelling at a velocity, c, will accelerate by U. If we assume, now, that the phase speed of the instability scales with the local velocity such that $c \sim U$ then the ratio of the time scales, which we will call the acceleration parameter, T_A, is then

$$T_A = \frac{t_g}{t_a} = \frac{\delta}{U} \frac{\mathrm{d}U}{\mathrm{d}x}. \tag{1.3}$$

This acceleration parameter is related to the inclination of the interface for hydraulically controlled flows, due to the baroclinic generation of vorticity. For channels involving only a variation in depth, $\mathrm{d}U/\mathrm{d}x$ is solely a result of baroclinic production. In cases where channel width varies, acceleration results from both baroclinic generation and cross-stream stretching of vorticity. This is discussed further in the Appendix.

The choice of velocity scale over which to define t_a is at our discretion, hence there is no requirement that $t_g \sim t_a$ and, equivalently, that $T_A \sim O(1)$. We will wish to examine then the variation of this parameter more than its absolute magnitude and we will quantify the effects of its variation on the mixing for three experimental geometries.

https://doi.org/10.1017/S002211209800250X Published online by Cambridge University Press

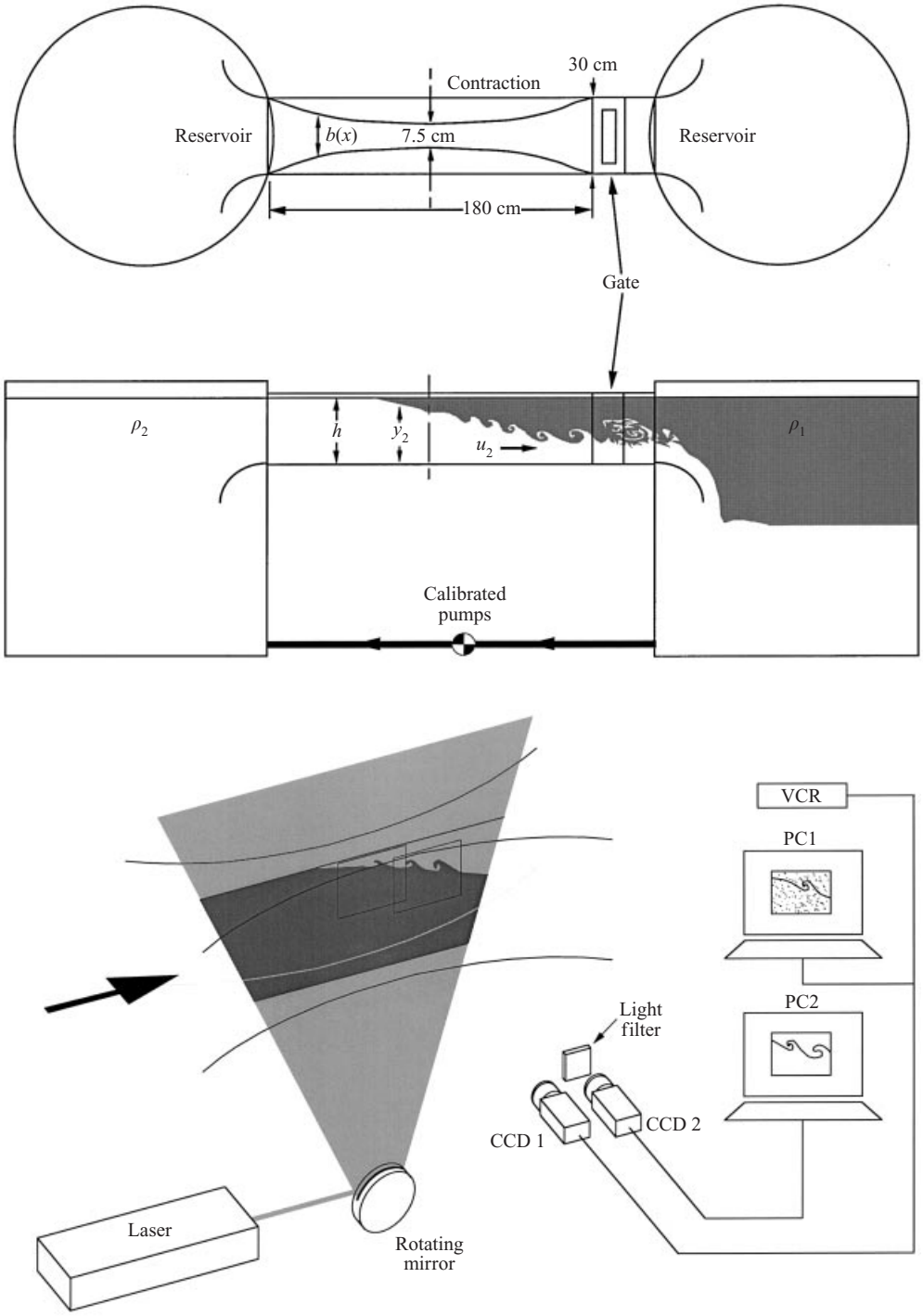


FIGURE 3. Experimental facility and data acquisition system.

https://doi.org/10.1017/S002211209800250X Published online by Cambridge University Press

2. Experimental facility and techniques

The experimental facility, composed of a Plexiglas convergent-divergent channel connecting two 800 l tanks, is shown in figure 3. The major portion of the channel consisted of a 180 cm long contraction, 30 cm high, 7.5 cm wide at the centre and 30 cm wide at the ends.

Density variations were obtained using salt, with temperatures monitored in each tank using digital thermistor thermometers to ensure thermal variations were minimal. Experiments were initiated with one reservoir filled with a layer of salt water beneath a layer of about 300 l of fresh water and the second reservoir completely filled with salt water. A sliding gate at one end of the channel initially separates the two reservoirs. To begin the experiment, the gate is lifted and a known net barotropic flow is then generated in the channel by pumping salt water from the layered reservoir to the other with calibrated pumps. Open cell foam diffusers were placed in each tank as well as in the upstream section of the channel in order to eliminate velocity fluctuations generated by the pumping. Further details of the experimental facility and its operation are given in Pawlak & Armi (1997).

Available run time for the facility is a function of the density difference and the desired barotropic flow rate. After an initial transient of 5 to 10 minutes, during which the arrested wedge evolves from the initial gravity current, about 20 to 25 minutes of run time was possible for most experiments before mixed fluid collecting in the downstream reservoir would intrude upstream into the test section or would be pumped into the upstream tank. Density differences and barotropic flow rates were chosen to maximize run times while maintaining shear layer Reynolds numbers at levels of interest. Typical Reynolds numbers near the location of onset of instabilities were about 100 based on the momentum thickness. Richardson numbers ($g'\delta/\Delta U^2$) based on the momentum thickness were about 0.01. The experiments discussed herein fall within the range of moderate barotropic flow as addressed in Pawlak & Armi (1997).

The rate of acceleration of the flowing layer is a function of the rate of expansion of cross-sectional area of the channel (Armi & Farmer 1986; Pawlak & Armi 1997). Variations in the acceleration parameter, T_A, can then be generated by examining different channel geometries. Three separate channel geometries were used to obtain different expansion rates, as shown in figure 4. The first configuration (figure 4*a*), which corresponds to the intermediate acceleration case, is the unaltered channel geometry using a symmetrical variation in width and a constant depth. A high acceleration case (figure 4*b*) was achieved by an increase in expansion through the introduction of a Plexiglas and foam sill along the channel bottom. The third geometry (figure 4*c*), a low acceleration case, reduced the expansion by adding a flat Plexiglas plate along one channel wall.

2.1. *Concentration measurements*

The density field was obtained by measurement of the fluorescence of Rhodamine 6G dye. The channel was illuminated from below with a vertical laser sheet aligned in the streamwise direction. The laser sheet was generated from an 8 W argon laser reflected off a rotating polygonal mirror beneath the channel (see figure 3). A CCD camera, positioned on a streamwise traverse about 1 m from the laser sheet, provided a view of roughly an 8 cm by 10 cm area of the channel at any streamwise location, with a 240 by 640 pixel resolution in each video field. Both horizontal and vertical camera orientations were used. A high-pass colour filter was used to eliminate reflections from particles seeded in the flow for particle imaging.

https://doi.org/10.1017/S002211209800250X Published online by Cambridge University Press

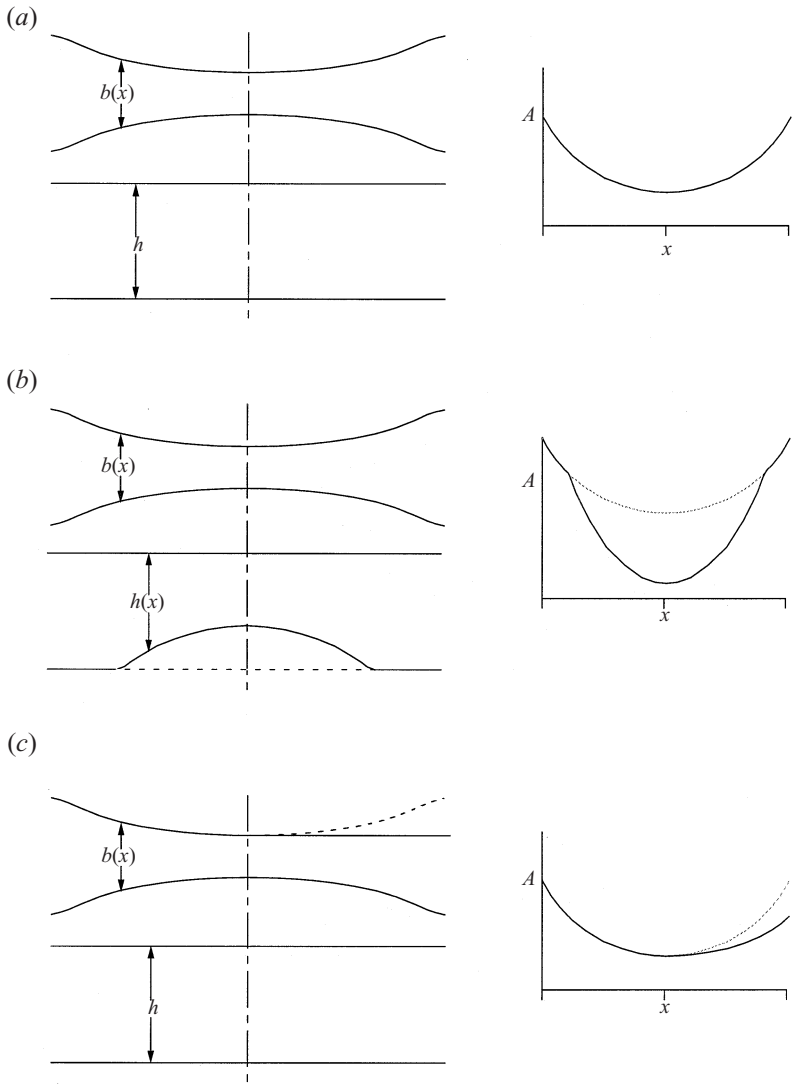


FIGURE 4. Plan and side views of channel geometries along with variation in cross-sectional area versus x. (*a*) Unaltered geometry (*b*) Increased expansion. (*c*) Reduced expansion.

Light reflected from the particles at the laser wavelengths was virtually eliminated by the filter, while the light generated by the rhodamine fluorescence suffered little attenuation.

The concentration of rhodamine was chosen to remain within the linear range of the luminescence–concentration relation. This was found to be satisfied at concentrations below 5.0×10^{-7} g cm^{-3} both by our own experiments and by a study by Lemoine, Wolff & Lebouche (1996). Rhodamine dye was mixed with the salt prior to the experiment, filling the tanks and channel with a homogeneous mixture. With the channel full of a uniform concentration of dye, images of the light sheet were digitized in order to obtain the spatial variation in the light field for normalization. Since the camera and the rotating mirror were both mounted on the traverse, this field remained the same at any streamwise position. Images at several vertical positions

https://doi.org/10.1017/S002211209800250X Published online by Cambridge University Press

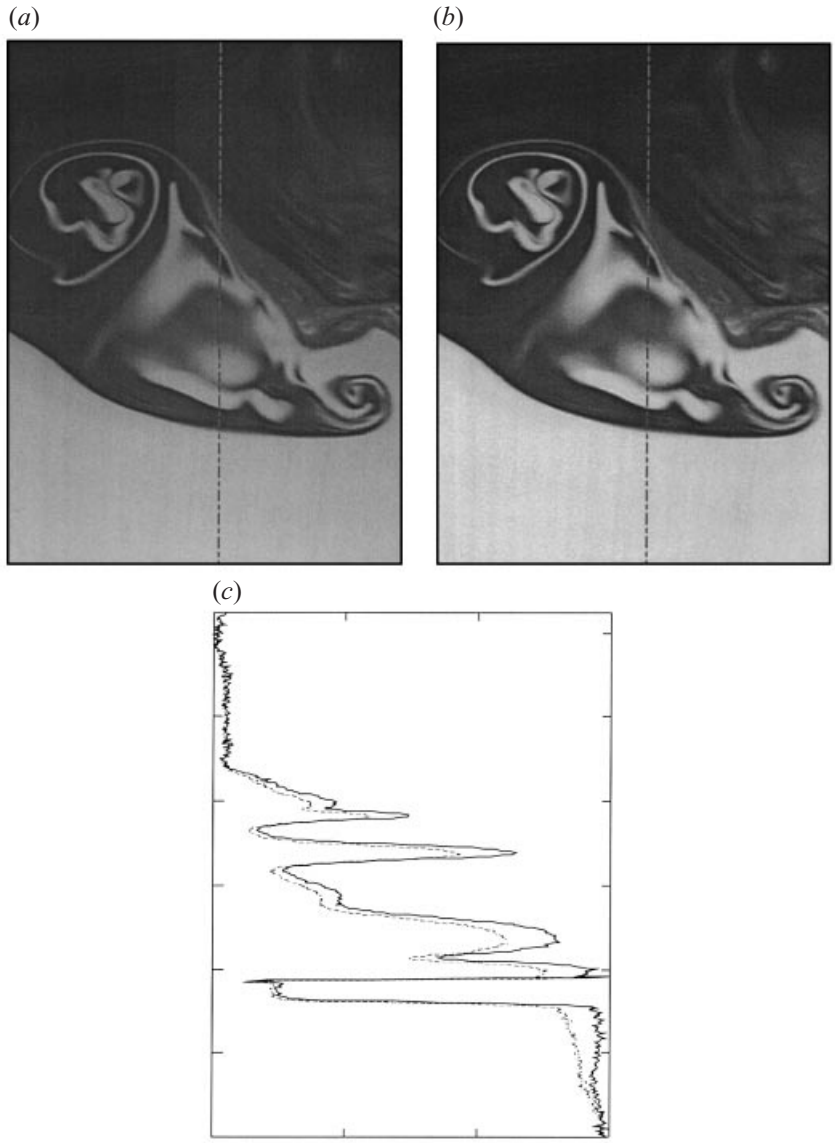


FIGURE 5. (*a*) Single image captured using the colour filter for concentration measurement. (*b*) Image corrected for spatial variation in laser sheet. (*c*) Plots of intensity along vertical cut in image (*a*) (solid line) and (*b*) (dashed line). Location of vertical cut is indicated in (*a*) and (*b*) by a dashed line.

were digitized and later pieced together digitally to obtain the full light field in the channel. Eight-bit greyscale images of the flow were then captured directly onto a PC at either 3 or 5 Hz allowing sequences of nearly a minute in length at a time. Figure 5(*a*) shows an individual greyscale image from one sequence. A reference grid is placed on the channel and a single frame is digitized prior to capturing the sequence. With the vertical position of the image identified, the corresponding normalization field can be obtained from the full light field. Figure 5(*b*) shows the normalized image which has eliminated the spatial variation in the laser sheet. Plots representing

https://doi.org/10.1017/S002211209800250X Published online by Cambridge University Press

intensity along a vertical cut from each image (identified by the dashed line in 5*a* and 5*b*) are shown in figure 5(*c*).

2.2. *Particle imaging velocimetry*

The low flow velocities (< 7 cm s^{-1}) made it possible to implement a simple digital particle imaging velocimetry system. A description of the method along with a detailed error analysis of the general technique is given by Fincham & Spedding (1997). A second CCD camera was positioned on the streamwise traverse to view a roughly 10 cm by 8 cm area just upstream of that viewed by the camera used for concentration measurement. At the velocities and resolutions of interest, the video synchronization rate of 30 Hz was adequate for imaging; pulsing of the laser sheet was not necessary. The video feed was captured directly onto a PC, allowing 7 s sequences of 640 by 480 pixel, 8-bit greyscale images at 30 Hz. Longer sequences at lower sampling rates were used for average measurements. The camera output was also recorded continuously onto Super VHS videotape for flow visualization and further DPIV analysis.

The captured 640 by 480 pixel images are separated digitally into 640 by 240 pixel even and odd fields, from which successive even frames are used for DPIV processing. The CCD camera used for the PIV analysis was set to integrate across two succesive rows of pixels in each field. In this manner maximum information is retained in the deinterlacing; however, the vertical resolution is half of the horizontal resolution. The DPIV algorithm utilizes cross-correlations between rectangular sections, or interrogation regions, from each image in a pair to obtain measurements of the local displacement. First, a rough estimate of the displacement is obtained using a course grid, with typical interrogation regions of 64 by 32 pixels at intervals of 48 by 24 pixels. A second correlation is then done using a finer grid, with regions of 12 by 24 pixels at intervals of 10 by 20 pixels. A region from the first image is correlated with a section of the second image, displaced by an interpolated value of the initial rough grid estimate. Sub-pixel estimates of the fine grid correlation peak are obtained with a two-dimensional Gaussian fit of a 3 by 3 pixel matrix around the initial approximation for the maximum.

Some image processing of the raw captured images was necessary prior to the DPIV processing in order to eliminate velocity biasing due to non-uniformities of the laser field in the fluorescent layer. Vertical shadows were produced occasionally by large particles along the channel bottom or from imperfections in the Plexiglas. These produce patterns in the image which tend to bias the correlation to a zero horizontal velocity. The images were first filtered using a course median filter to eliminate the high-frequency signal from the particles. The filtered image is then subtracted from the original to retrieve the particle field. Inevitably, some sub-pixel error is introduced through the median filtering; however, the method allows us to successfully eliminate the biasing due to the shadows. Velocity fields obtained from the DPIV analysis were used to obtain shear layer data in the upstream region, free-stream average velocities, vorticity fields and streamlines.

3. Experimental observations

Experiments were run over a range of barotropic flow conditions with the unaltered channel geometry and although there were slight differences in the scale and growth rate of instabilities in each case, the general mechanism proved to be quite robust, showing little qualitative change.

In all of the experiments, shear layer Reynolds numbers were such that the interface

https://doi.org/10.1017/S002211209800250X Published online by Cambridge University Press

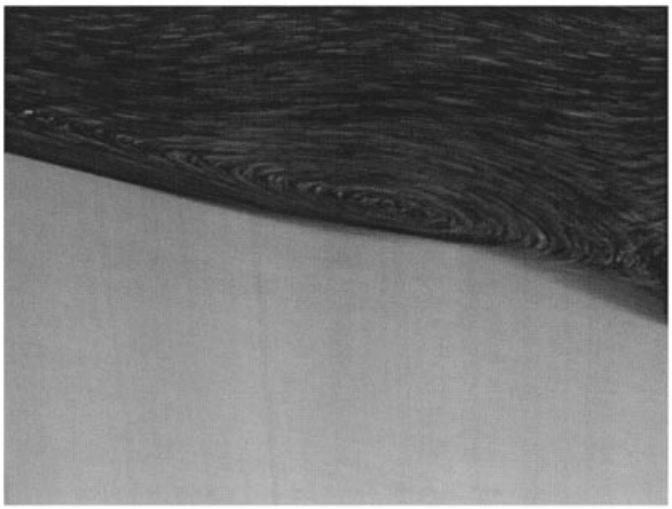


FIGURE 6. One second time lapse of flow at onset of instability.

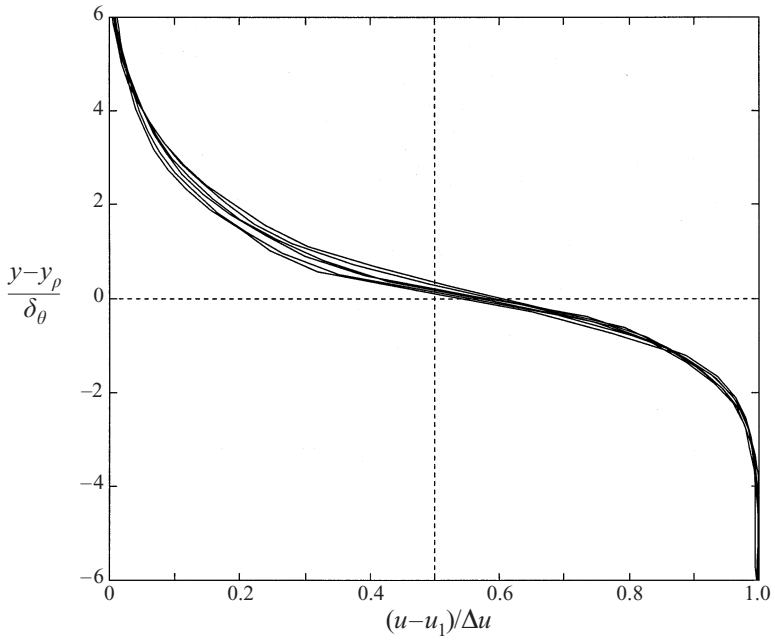


FIGURE 7. Experimental velocity profiles just prior to onset of instability. Vertical coordinate is referenced to density interface (y_ρ) and is non-dimensionalized by the momentum thickness, δ_θ. Velocity is measured relative to the velocity of the low-momentum stream (u_1) and non-dimensionalized by the total shear, ΔU.

remained stable in the upstream subcritical region. The region in the vicinity of the tip of the wedge was marked by a three-dimensional cross-stream structure, primarily due to boundary layer and surface tension effects; however, the interface profile quickly became uniform across the channel as the interface deepened and as the flow transitioned to supercritical conditions.

Interfacial instabilities began between 20 and 40 cm from the tip of the wedge as

https://doi.org/10.1017/S002211209800250X Published online by Cambridge University Press

FIGURE 8

FIGURE 9



FIGURE 8. Image (left-hand column) and vorticity (right-hand column) sequence at onset of instability for intermediate acceleration case. Each frame is a 0.1 s average at intervals of 0.5 s. Physical dimensions of the images are approximately 10 cm × 7.5 cm. Vorticity scale is shown with the colourbar with units of 1/s.

FIGURE 9. Image (left-hand column) and vorticity (right-hand column) sequence from intermediate acceleration case showing initial separation and pinching off of core region. Each frame is a 0.1 s average at intervals of 0.5 s.

https://doi.org/10.1017/S002211209800250X Published online by Cambridge University Press

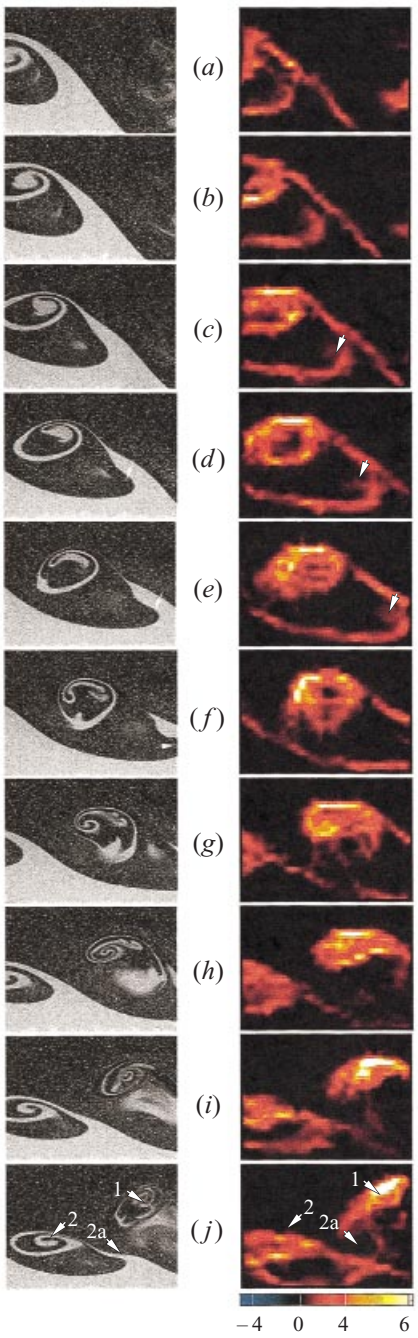


FIGURE 10. Image (left-hand column) and vorticity (right-hand column) sequence showing pinching off of core and modified pairing mechanism. Each frame is a 0.1 s average at intervals of 0.5 s.

oscillations of the interface, rapidly growing downstream. The location and frequency of the initial instabilities remained quite constant with only a slow oscillation of about 10 to 15 cm in the generation position occurring over the course of an experiment.

The initial stages of finite-amplitude growth exhibit significant asymmetry, with a

https://doi.org/10.1017/S002211209800250X Published online by Cambridge University Press

bias of the vortex centre into the stagnant upper layer. Figure 6 shows an average of images over 1 s at the location of the initial instability from the intermediate acceleration case, revealing the centre of rotation of the instability displaced above the interface. Flow is from left to right with the stagnant layer on the top. Average velocity profiles obtained from DPIV analysis just upstream of the location of initial instability, presented in figure 7, show no significant offset between the centres of the density and the velocity profiles. The density interface at this location is essentially a step centred at zero.

Figures 8, 9 and 10 present image sequences† of the finite-amplitude development of the shear instability along with vorticity fields for each image. The sequences represent successive stages of spatial development of the mixed layer. Each sequence was obtained at different times, but due to the regular interval and repeatability of the instabilities, we can utilize them to construct a spatial picture of the development of a single vortex. The frame interval for each sequence is 0.5 s with the vorticity fields each representing a 0.1 s average.

The early frames in figure 8 show fluid from the fast moving stream being drawn rapidly into the vortex core and wound up in the shape of the familiar finite-amplitude Kelvin–Helmholtz billows. An asymmetry in the developing core is apparent in frame (*e*). The bias of the centre of the vortex core, indicated by the arrow in frame (*f*), can already be clearly discerned in the ensuing image and vorticity frames.

At this stage the development deviates from that of the traditional non-accelerating shear layer. Figures 9 and 10 illustrate the subsequent altered phase of the finite-amplitude growth. In figure 9, the entire vortex structure elongates in the direction of the flow, primarily drawing fluid from the stagnant upper region into the billow. The core begins to lag behind the braid as the acceleration continues. The term 'braid', here, refers to the narrow region of density gradient near the stagnation point occurring between successive vortices (Corcos & Sherman 1976). The vortex core has become further separated from the rest of the instability in figure 10 and a new core region is observed to develop (identified by the arrows in figure 9*e* and figure 10*c–e*) while the old core eventually pinches off and is left behind. In its place, a secondary core begins to form. The original core continues to convect slowly downstream and interacts with the following upstream structure. A strong subharmonic component is observed, with alternate rollups being displaced towards the faster moving stream (figure 10*h–j*), while still exhibiting the separation and pinching off mechanism followed by the formation of a secondary core. The individual coherent vortices are identified in figure 10(*j*) with the original core labelled as structure # 1, the following core is structure # 2 and the secondary core is structure # 2a. The interaction further downstream between the original core of the first structure in the subharmonic pair and the second structure is a modified form of pairing event, with the original core amalgamating with both the following pinched off core and its secondary core.

A variation of this pairing is also observed involving a shredding interaction where a portion of the old core is torn off and amalgamates with the second structure and the remaining portion of the original core survives in the low-momentum side until it interacts with a third vortex. We call this type of interaction a 'leapfrog' pairing. An image sequence of a typical pairing interaction is shown in figure 11. The sequence was obtained from a separate experiment with the nominal geometry and

† Complete video sequences of the images and corresponding vorticity fields presented in this paper, along with additional examples are available on CD-ROM in standard formats. Interested readers should contact the authors or the Journal of Fluid Mechanics Editorial Office.

https://doi.org/10.1017/S002211209800250X Published online by Cambridge University Press

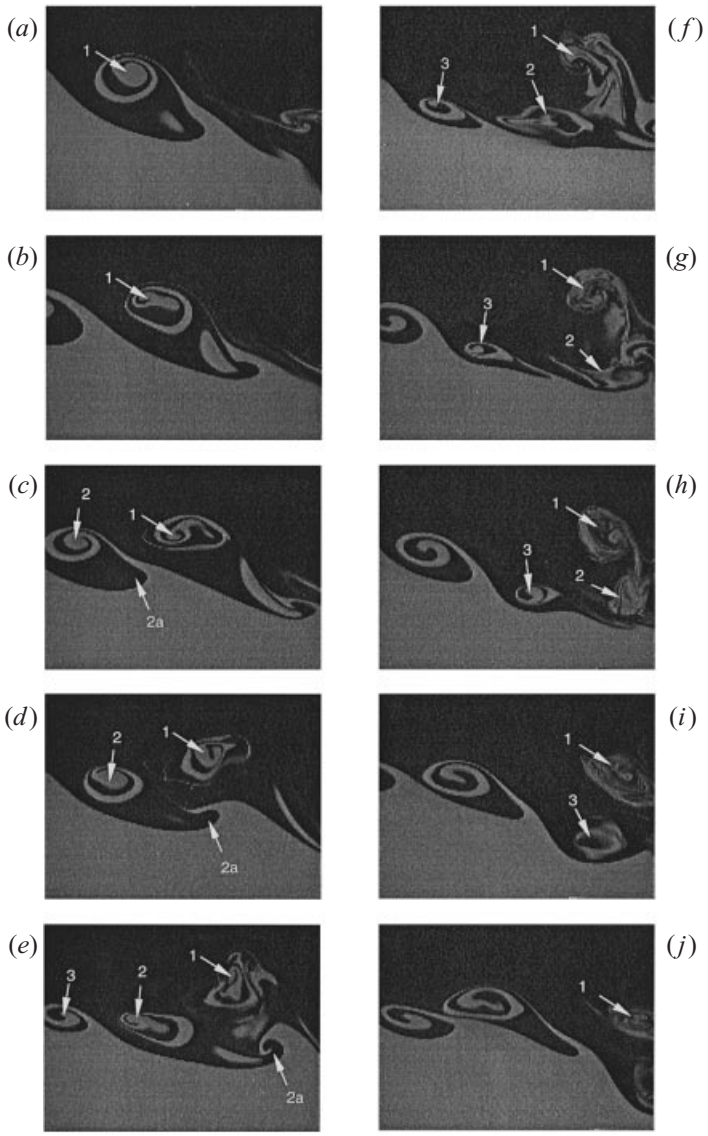


FIGURE 11. Image sequence of typical vortex pairing interaction. Flow parameters correspond to those of the intermediate acceleration. Imaged area is approximately 15 cm × 11 cm. Frame interval is 1.5 s.

flow parameters but with a larger image field visualized. The initial separating core, identified as vortex #1 in the sequence, can be followed through the sequence as it 'leapfrogs' the next vortex in the subharmonic pair (#2) along with its secondary core (#2a). Only a portion of vortex #1 appears to tear off in frame (*f*) and amalgamate with vortex #2 and #2a, but a significant part remains in frames (*h–j*) even after the third vortex (#3) has passed below.

Further downstream, in the more fully developed region of the mixing layer, there is evidence of the persistence of the vortex mechanism illustrated in figures 8–10. An image and vorticity sequence from this region is shown in figure 12. The imaged area covers approximately two-thirds of the average shear layer thickness (as determined

https://doi.org/10.1017/S002211209800250X Published online by Cambridge University Press

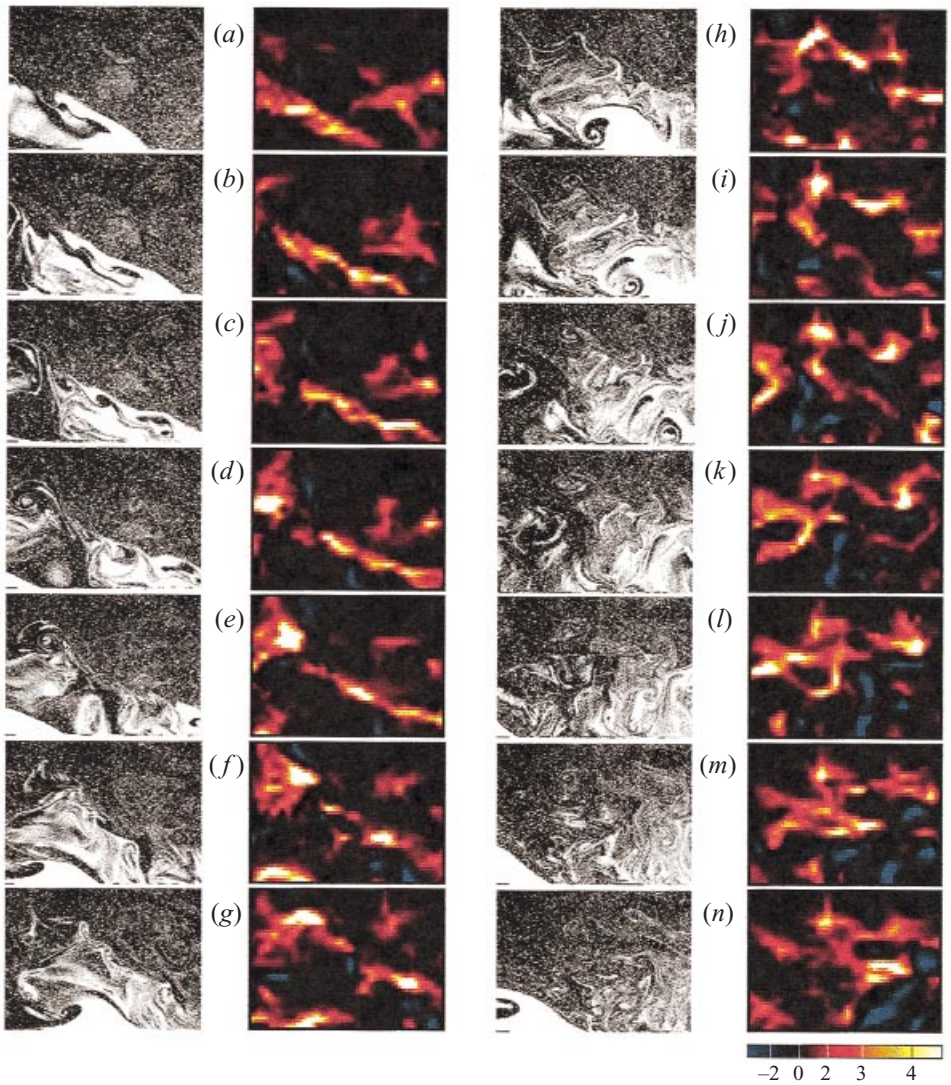


FIGURE 12. Image (left-hand column) and vorticity (right-hand column) sequence from fully developed region of intermediate acceleration case showing evidence of separation and pinching mechanism.

from fluorescence density measurements) and is roughly aligned with the centre of the density profile. In the initial frames, there is little visible evidence of mixing in the upper portion of the image; however, the corresponding vorticity fields reveal significant areas of vorticity. A vortex structure can be observed entering from the left of the image. As this structure convects through, it leaves a trail of vorticity behind which extends upward ending in a core of concentrated vorticity visible in frame (*d*). Note that the vorticity associated with the initial structure is relatively weak in comparison to that in the trailing core. The bulk of available vorticity has been removed in the separated core, leaving only the newly generated vorticity near the high-momentum stream. This process will be further addressed in § 5. The separated core survives in the imaged region well after the leading structure has left the field of view. A second trailing structure is visible entering in frame (*k*). This amalgamates

https://doi.org/10.1017/S002211209800250X Published online by Cambridge University Press

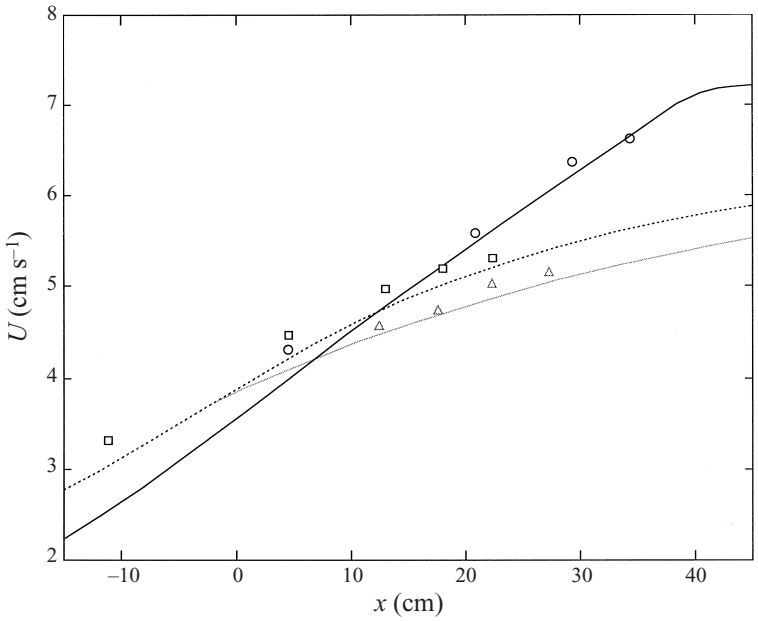


FIGURE 13. Free-stream velocity vs. downstream position (referenced relative to the narrowest section) for $T_A = 0.0012$ ($\cdots\cdots\triangle$), $T_A = 0.003$ ($- - - -\square$) and $T_A = 0.0046$ (——○). Lines indicate predictions from hydraulic theory and individual points represent average experimental measurements using PIV. Velocity are accurate to within ± 0.1 cm s^{-1} for the low and intermediate acceleration case and ± 0.2 for the high acceleration case.

with much of the first separated core, although a smaller remnant of the original is still visible in the final frame.

3.1. *Alternative channel geometries*

The effect of various rates of acceleration on the vortex mechanisms was examined through the use of the alternative channel geometries discussed in § 2. The geometries, density steps, g', and barotropic flow rates, U_0, were chosen using hydraulic theory predictions for velocities (Pawlak & Armi 1997) with the goal of maintaining the magnitude of velocities at the region of instability development at comparable values for each case. Theoretical velocity predictions for each experiment along with experimentally measured values using PIV are summarized in figure 13. Free-stream velocities fluctuated as much as 8% for the intermediate and low acceleration cases and 12% for the high acceleration case, due to the passing of vortices in the mixed layer. Averaging over a minute of data (10 to 20 occurrences) allowed estimates of average velocity to within $2-4\%$. Velocities upstream are comparable for the three cases, with variations occurring in the downstream (unstable) portion.

The value of the acceleration parameter, T_A, as defined by equation (1.3), was evaluated for each of the three geometries at the location of initial instability. We have chosen the momentum thickness, δ_θ, defined as

$$\delta_\theta = \frac{1}{u_2 - u_1} \int_{-\infty}^{\infty} (u_2 - u(y))\,(u(y) - u_1)\,\mathrm{d}y \tag{3.1}$$

as the representative vertical length scale, where u_1 and u_2 are the low- and high-momentum stream velocities, respectively. While we will use these values of T_A

https://doi.org/10.1017/S002211209800250X Published online by Cambridge University Press

T_A	h_0 (cm)	g' (cm s^{-2})	U_0	x_i (cm)	y_i (cm)	u_i (cm s^{-1})	F_i^2	δ_{θ_i} (cm)
0.0012	20.0	1.3	0.56	10	14.2	4.4	1.05	0.17
0.0030	20.0	1.3	0.55	10	12.0	4.7	1.42	0.26
0.0046	12.5	1.8	0.55	20	5.3	5.5	3.17	0.28

TABLE 1. Experimental parameters: T_A, non-dimensional acceleration parameter; h_0, total channel depth at narrowest section; g', reduced gravity; U_0, non-dimensional barotropic flow rate; x_i, streamwise location of onset of instability; y_i, interface depth at $x = x_i$; u_i, layer velocity at $x = x_i$; F_i^2, Froude number at $x = x_i$; δ_{θ_i}, momentum thickness at $x = x_i$.

to identify each of the cases considered, it should be apparent that T_A is a local parameter and an integral value would be more appropriate, for example, when considering mean profiles of momentum and density, as we shall discuss in § 5. Values for the relevant quantities at the onset of instability along with flow parameters at the narrowest section (which serve to determine the background hydraulic flow) are listed in table 1. The position of onset of instability, x_i, is an approximate value based on observations over the course of each experiment. The non-dimensional barotropic flow rate is given as $U_0 = q_f/b_0h_0(g'h_0)^{1/2}$, where the subscript 0 indicates values at the narrowest section of the channel and q_f is the net volume flow through the channel. The Froude number, $F^2 = u^2/g'y$ is a measure of the criticality of the flow relative to long internal waves.

For the high acceleration geometry ($T_A = 0.0046$), which included a variation in depth (figure 4*b*), a slightly higher density step of $g' = 1.8$ was necessary to maintain velocities consistent with the unaltered case. Since velocities scale with $(g'h_0)^{1/2}$, the higher value of g' offset the reduction in depth at the narrowest section. Instabilities again exhibited a very regular generation location and frequency. Figure 14, left-hand column, shows an image sequence for $T_A = 0.0046$ in the region of finite-amplitude development. The frames show a very similar mechanism to that observed in the unaltered case, with more distinct features apparent. The developing vortex core detaches from the interface and a new vortex core begins to develop. The secondary core (refer to frames *c* and *f* in figure 14 on the left) shows increased development relative to the same stage for $T_A = 0.003$ (frames *c* and *i* in figure 14 on the right). In addition, the interaction between the original core from the first structure in the subharmonic pair and the secondary core from the second occurs at a position further upstream.

The low acceleration case ($T_A = 0.0012$), resulting from a less rapid expansion in width downstream of the narrowest section with no variation in depth (figure 4*c*), required a density step of $g' = 1.3$ to obtain the necessary velocities. The laser sheet was angled slightly in the cross-stream plane to minimize out of plane motion resulting from the channel asymmetry. Initial development of the instabilities was consistent with the higher T_A cases, with similar vortex separation occurring. The interface angle and subsequent vortex separation was less than that observed in the other two cases.

Time-averaged density profiles were obtained for each experiment at various downstream locations using the methods described in § 2. Figure 15 shows vertical density profiles at equivalent downstream locations for each experiment, corresponding to points just downstream of the initial pairing or vortex separation location. The profiles show increasing asymmetry with higher accelerations. Profiles for $T_A = 0.003$ and $T_A = 0.0012$ (figures 15*a* and 15*b*) are characterized by a sharp step near the high-momentum stream with a long low-gradient tail extending into the low-momentum

https://doi.org/10.1017/S002211209800250X Published online by Cambridge University Press

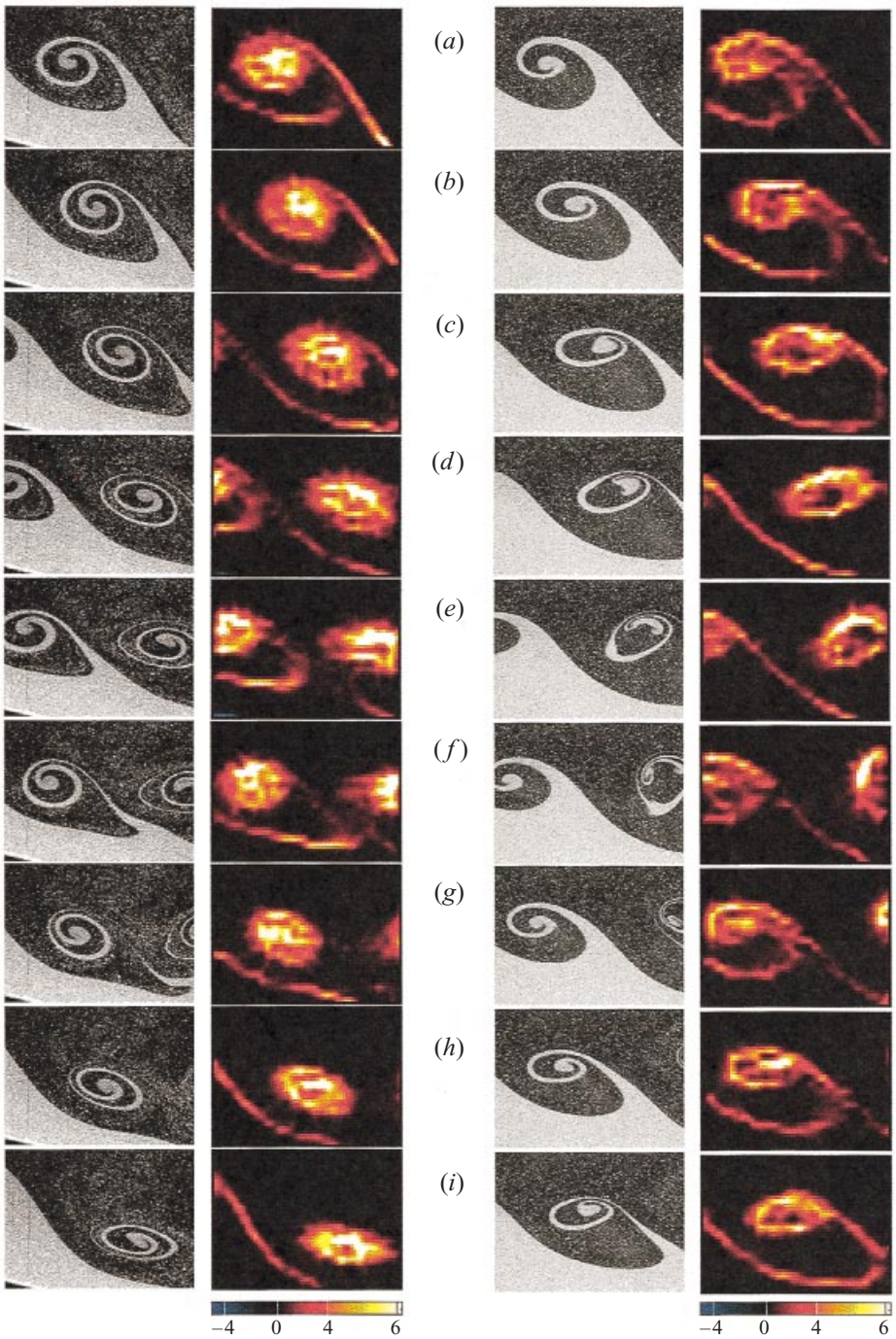


FIGURE 14. Image and vorticity sequences for high acceleration case ($T_A = 0.0046$) (left-hand columns), intermediate case ($T_A = 0.003$) (right-hand columns).

https://doi.org/10.1017/S002211209800250X Published online by Cambridge University Press

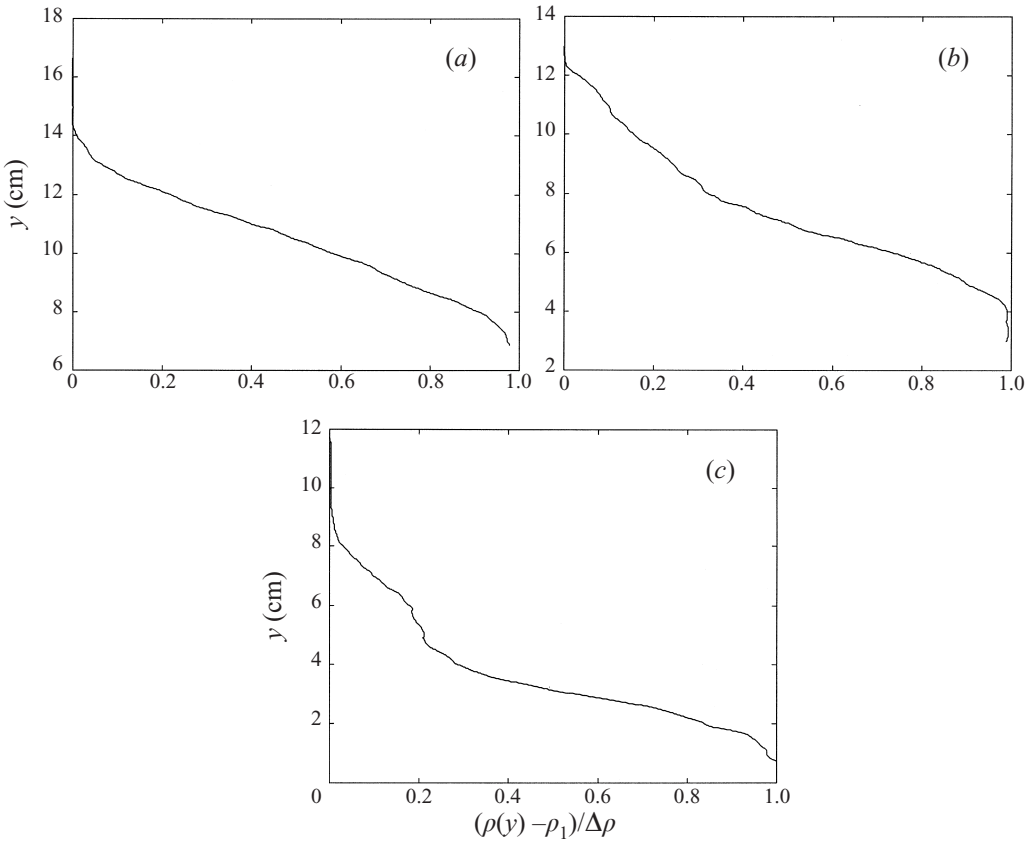


FIGURE 15. Normalized density profiles just downstream of a pairing event versus height from channel bottom. (*a*) $T_A = 0.0012$. (*b*) $T_A = 0.003$. (*c*) $T_A = 0.0046$.

region. The lower acceleration case (figure 15*c*) results in a more symmetric profile. Differences in these profiles will be discussed in more detail in § 5.

4. Spatial linear stability analysis

In order to investigate the instability modes possible and to gain some insight into the initial stages of the mechanism observed, a spatial linear stability analysis is presented here. With this purpose in mind, we will consider a parallel flow, under the assumption that the acceleration does not significantly affect the nature of the possible modes. Experimental observations will be used to validate this assumption. The effects of acceleration, along with the assumption of inviscid flow make absolute quantitative comparisons with experimental results difficult; however, the analysis remains an instructive and necessary part of the phenomenological description we are constructing.

The stability of infinitesimal perturbations in an inviscid, incompressible, stratified, parallel shear flow is governed by the Taylor–Goldstein equation. For Boussinesq flow, this is given by

$$\frac{\partial^2 v}{\partial y^2} + \left(\frac{N(y)^2}{(U(y)-c)^2} - \frac{\partial^2 U/\partial y^2}{U(y)-c} - k^2 \right) v(y) = 0, \tag{4.1}$$

https://doi.org/10.1017/S0022112098002500X Published online by Cambridge University Press

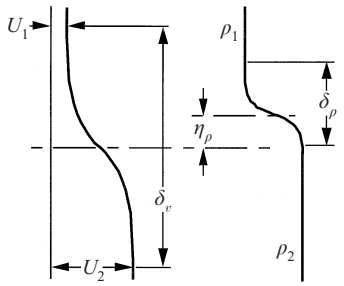


FIGURE 16. Generalized velocity and density profiles.

where $U(y)$ is the vertical profile of the x velocity, $v(y)$ is the complex modulus of the vertical perturbation velocity, $N(y)$ is the buoyancy frequency, k is the wavenumber and $c = \sigma/k$ is the complex phase speed, with σ being the frequency. We choose our vertical length scale as the shear layer momentum thickness, δ_θ, and the velocity scale as one half of the shear, $\Delta U = U_2 - U_1$. Following Hazel (1972) we use $\hat{y} = y/2\delta_\theta$ as the vertical coordinate with the dimensionless wavenumber, $\alpha = 2k\delta_\theta$, the dimensionless frequency, $\beta = 2\sigma\delta_\theta/\Delta U$ and define the density profile by

$$\rho = \rho_0 \exp\left(-\frac{\Delta\rho}{\rho_0} S(\hat{y})\right) \tag{4.2}$$

with

$$S = \tanh\left(R(\hat{y} - \eta_\rho)\right)$$

where $\Delta\rho = (\rho_2 - \rho_1)$ is the overall density step, $\rho_0 = \frac{1}{2}(\rho_1 + \rho_2)$ and η_ρ is the offset of the density interface from the velocity interface (see figure 16). We allow for a variation in the ratio of velocity to density scales through the ratio $R = \delta_\theta/\delta_\rho$. The velocity profile is given by

$$\hat{u} = \frac{2U(y)}{\Delta U} = \frac{2U_1}{\Delta U} + (1 + \tanh(\hat{y})). \tag{4.3}$$

Dropping hats on the dimensionless variables, the dimensionless Taylor–Goldstein equation is then

$$\ddot{v} + \left(\frac{J\dot{S}}{(u - \beta/\alpha)^2} - \frac{\ddot{u}}{(u - \beta/\alpha)} - \alpha^2\right) v(y) = 0, \tag{4.4}$$

where dots indicate derivatives in y and $J = 8g'\delta_\theta/\Delta U^2$ is the bulk Richardson number. J is also equivalent to the Richardson number at the origin for the case of $\eta_\rho = 0$.

We will consider the case of a shear flow with rigid boundaries located at $y = y_1$ and $y = y_2$ where the disturbance velocity must vanish. The necessary boundary conditions are then given by

$$v = 0 \quad \text{at} \quad y = y_1, y_2. \tag{4.5}$$

For a given velocity profile, $u(y)$, density profile, $S(y)$, bulk Richardson number, J, and wavenumber, α, the solution of the linear stability problem is an eigenvalue for either a complex frequency, β, or a complex wavenumber, α, for which the eigenfunction, $v(y)$ satisfies the prescribed boundary conditions at $y = y_1, y_2$. Choosing the frequency as the eigenvalue is equivalent to considering a temporally growing disturbance, while the choice of α as the eigenvalue considers the case of a spatially growing instability.

https://doi.org/10.1017/S002211209800250X Published online by Cambridge University Press

Although the temporal problem has traditionally received greater attention, the spatial problem is more directly relevant to spatially developing shear flows such as that in the present study and as such, we will investigate the case of a complex wavenumber, $\alpha = \alpha_r + \mathrm{i}\alpha_i$.

Equation (4.4) along with the necessary boundary conditions, (4.5), was solved numerically for α using a finite difference approximation employing a two-dimensional shooting method.

We shall examine solutions obtained using boundary conditions and parameter values corresponding to those at the onset of instability for the unaltered flow case. These are: $\eta_\rho = 0$, $U_1 = -0.3$ cm s^{-1}, $U_2 = 4.5$ cm s^{-1}, $\delta_\theta = 0.25$ cm, $y_1 = 8.0$ cm, $y_2 = -12.0$ cm. A more general analysis over the (J, α) plane along with a study of the effects of an offset of the density interface ($\eta_\rho \neq 0$) is given in § 4.2.

The appropriate value for the ratio of velocity to density scales, R, is primarily a function of Schmidt number, Sc, for salt in water, such that

$$R \sim Sc^{1/2} \simeq 16; \tag{4.6}$$

however, the existence of a viscous layer upstream of the wedge tip would suggest a higher value for R. We have chosen a value of $R = 50$ for the results presented here, although further study reveals very little change in the solutions for $R > 8$.

4.1. *Modes of instability*

Two relevant solution types were obtained for the given conditions at each real wavenumber, α_r. The fastest growing mode, which we will call mode A, corresponded to a wavenumber, $\alpha = 0.60 - 0.22\mathrm{i}$ with a phase speed of $c = 1.37$ cm s^{-1}. For the same real wavenumber, a slower growing solution ($\alpha_i = -0.09$), mode B, was found, with a higher phase speed of $c = 2.87$ cm s^{-1}. These modes are analogous to the positive and negative Holmboe instabilities which are found as solutions to the temporal problem (Hazel 1972; Lawrence *et al.* 1991). Solution A corresponds to the upstream propagating, or negative solution. The slower growing solution B relates to the positive temporal solution, with its slower growth rate a result of the higher phase speed. The fastest growing solution for mode B occurred at a wavenumber of $\alpha = 0.81 - 0.09\mathrm{i}$. It should be noted that the growth rates and phase speeds for the spatial problem are not equivalent to the linearly transformed solutions from the temporal case. The distinction between the dispersive Holmboe mode and the non-dispersive Kelvin–Helmholtz mode illustrates the difference in the two approaches. There is no clearly defined criterion to distinguish between the Holmboe mode and the Kelvin–Helmholtz mode in the spatial case. The analysis of the spatially developing unstratified shear layer by Michalke (1965) found a single dispersive mode, in contrast to the classic temporal solution which has one non-dispersive Kelvin–Helmholtz mode. Our solution of (4.4), in fact, does not find any non-dispersive modes over the (J, α)-plane. As such, we will call our solutions hybrids of the Kelvin–Helmholtz and Holmboe modes.

Using the eigenfunctions, $v(y)$, corresponding to the solutions of (4.4) for modes A and B, and using the continuity relation, we can obtain a perturbation velocity field $u'(y)$ and $v'(y)$ of arbitrary amplitude. With this we can draw streamlines for the instability modes for a given instant in time. Streamline plots for modes A and B are displayed in figure 17. With $y = 0$ representing the centre of the velocity and density interfaces, and $y < 0$ being the high-momentum stream, the respective offsets of either mode is evident. The faster growing mode A shows significant displacement

https://doi.org/10.1017/S002211209800250X Published online by Cambridge University Press

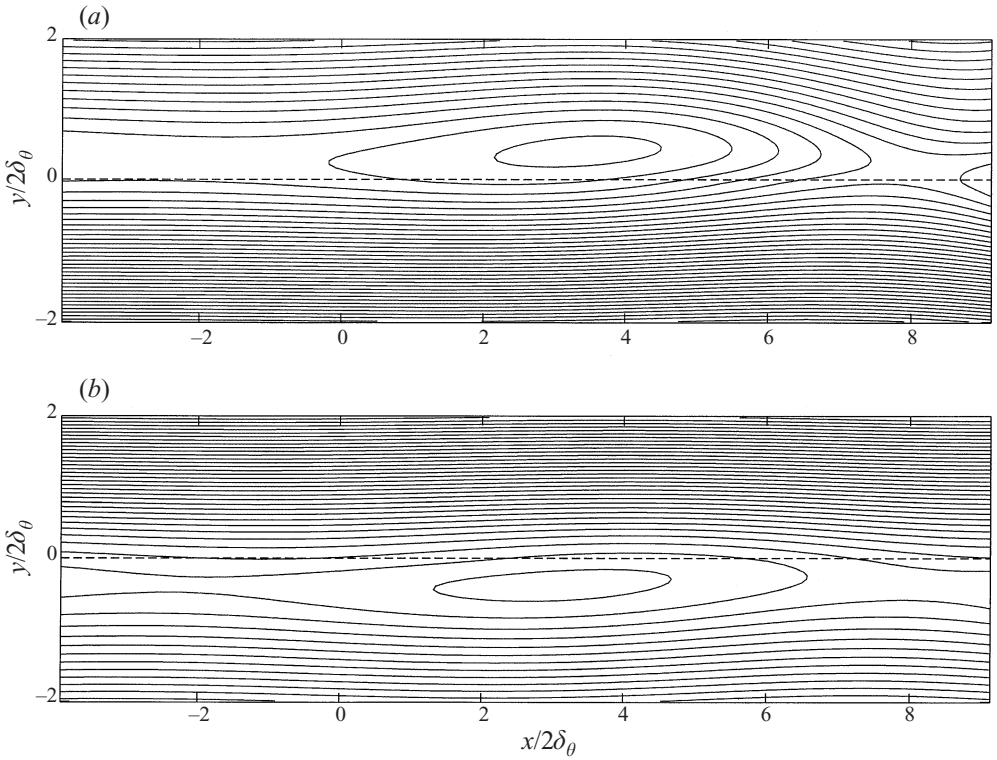


FIGURE 17. Streamlines of instability modes: (*a*) Mode A, (*b*) Mode B.

of its centre of rotation into the low-momentum side, while mode B is characterized by a less significant bias into the higher momentum stream.

4.2. *Effect of density offset*

The effect of a non-zero value of η_ρ was considered for the temporal case by Lawrence *et al.* (1991). We will examine the effect of the offset between the density and velocity interfaces on the linear stability of the spatially developing shear flow by considering eigenvalue solutions to (4.4). Density and velocity profiles are given by (4.2) and (4.3), respectively, with coordinates defined as shown in figure 16. The ratio of scales was chosen as $R = 50$, as discussed earlier. Disturbance velocities are required to vanish at equivalent non-dimensional vertical locations of $\hat{y} = \pm 20.0$. Solutions were examined for the case of $\eta_\rho = 0$ over a significant portion of the (J, α)-plane. Two relevant solutions were obtained and growth rates for these are shown in figure 18. The eigenvalue identified in § 4.1 as solution A, is dominant for all values of Richardson number, J. We will examine the effect of the offset by considering the (α_i, α_r)-plane at $J = 0.10$.

The variation of growth rates for each mode is summarized in figure 19. The qualitative behaviour of the solutions is similar to that predicted for the temporal case by Lawrence *et al.* (1991). The slower propagating solution A is characterized by a bias into the slower stream as illustrated in the streamline plot in figure 17(*a*) along with a higher spatial growth rate for $\eta_\rho = 0$. An offset of the density interface into the low-momentum stream results in a decrease in growth rate along with an increase in the most unstable wavenumber, with an offset in the opposite direction having the reverse effect. Mode B, represented by the streamline plot in figure 17(*b*), undergoes

https://doi.org/10.1017/S002211209800250X Published online by Cambridge University Press

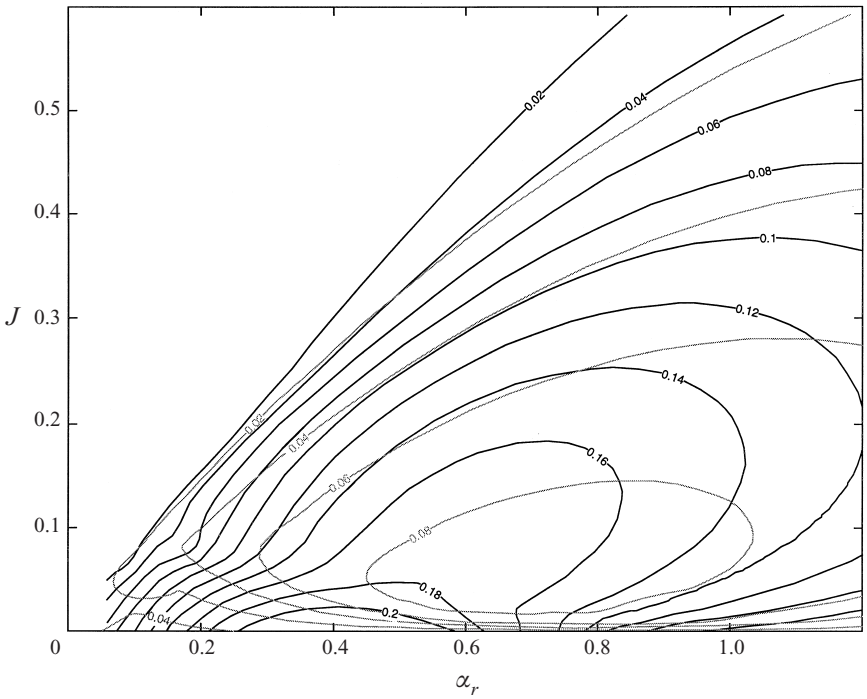


FIGURE 18. Spatial growth rates for modes A and B in the (J, α)-plane for $R = 50$, $\eta_\rho = 0$. Mode A is shown as solid black lines with mode B represented by the grey lines.

an increase in growth rate and a decrease in the fastest growing wavenumber for a positive η_ρ. Mode A remains the fastest growing solution for values of $\eta_\rho < 0.4$.

Both the temporal and spatial analyses indicate that the addition of a moderate density offset ($|\eta'_\rho| < 1.0$) results in the strengthening of one of the two hybrid modes. A negative offset (into the higher momentum stream) will result in an increase in growth rate and a decrease in most unstable wavenumber for mode A with the opposite effect on mode B. The slight negative offset apparent in figure 7 will have the effect of further reinforcing the dominance of mode A in the intermediate acceleration case.

4.3. *Effect of boundaries*

The introduction of rigid horizontal boundaries on a temporally developing shear layer was examined by Hazel (1972) for $R = 1$. The primary effect of the presence of boundaries is the destabilizing of lower wavenumbers. The most unstable wavenumbers remain largely unaffected until the boundaries are within less than $2.5\delta_\theta$ of the interface, after which all wavenumbers are gradually stabilized. The effect of boundaries will no doubt have a significant effect on the flow near the wedge tip for higher Reynolds number flows, but we shall not consider these effects since for all experimental cases discussed, the interface was quite deep at the point of initial instability.

5. Discussion

The flow visualization and DPIV results allow us to construct a cartoon of the vortex mechanics involved in the accelerating shear layer, motivated by the similar cartoon of the unaccelerated shear layer by Corcos (1988). The evolution of the mechanism is summarized in figure 20.

https://doi.org/10.1017/S002211209800250X Published online by Cambridge University Press

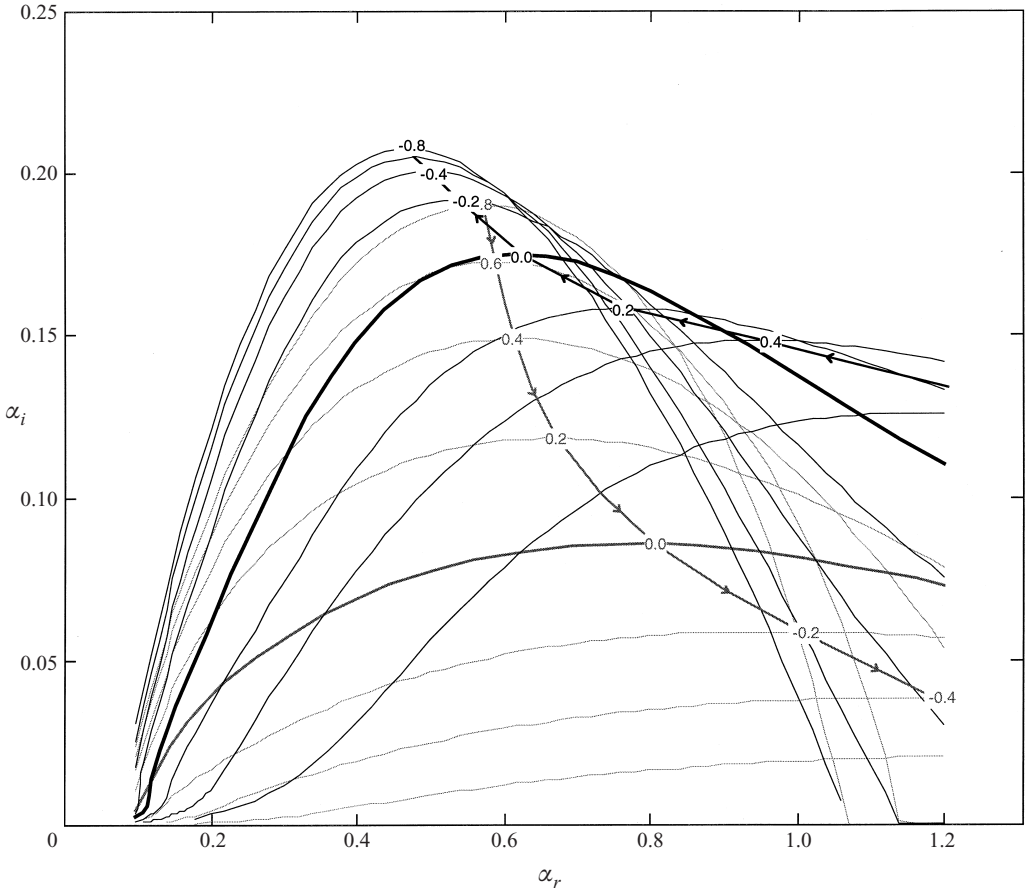


FIGURE 19. Variation of growth rates with η_ρ for modes A (solid lines) and B (grey lines).

The linear stability analysis has accounted for the initial bias of the centre of rotation of the instability into the low-momentum region. Comparison of the experimentally observed instability in figure 6 to the streamline plot for solution A in figure 17 validates the predictions of the linear analysis. Solution A has been shown to be the dominant mode over a range of conditions and we can then expect that this bias will be a regular feature of spatially developing flows in which the density interface is such that $R \gg 1$.

As the instability develops, it entrains fluid from the high-momentum side around its centre. The offset of the core centre from the interface results in a greater amount of low-momentum fluid being drawn into the developing core (figure 20*b*, *c*). The hybrid instability develops into a familiar billow structure concentrating the existing vorticity near its centre with new vorticity produced in the braid region continuing to feed into the core from either stagnation point. At this stage the effect of the acceleration becomes important. While the core continues to convect downstream at near its initial velocity, the high-momentum side of the structure is accelerated downstream. This elongates the structure in the streamwise direction, resulting in the separation of the developing core from its vorticity source in the downstream braid. This is visible in figure 20(*d*).

An additional buoyancy effect also plays an important role. The vortex core, as a coherent structure, is less dense than the fluid below it and, therefore, descends at a

https://doi.org/10.1017/S002211209800250X Published online by Cambridge University Press

https://doi.org/10.1017/S002211209800250X Published online by Cambridge University Press

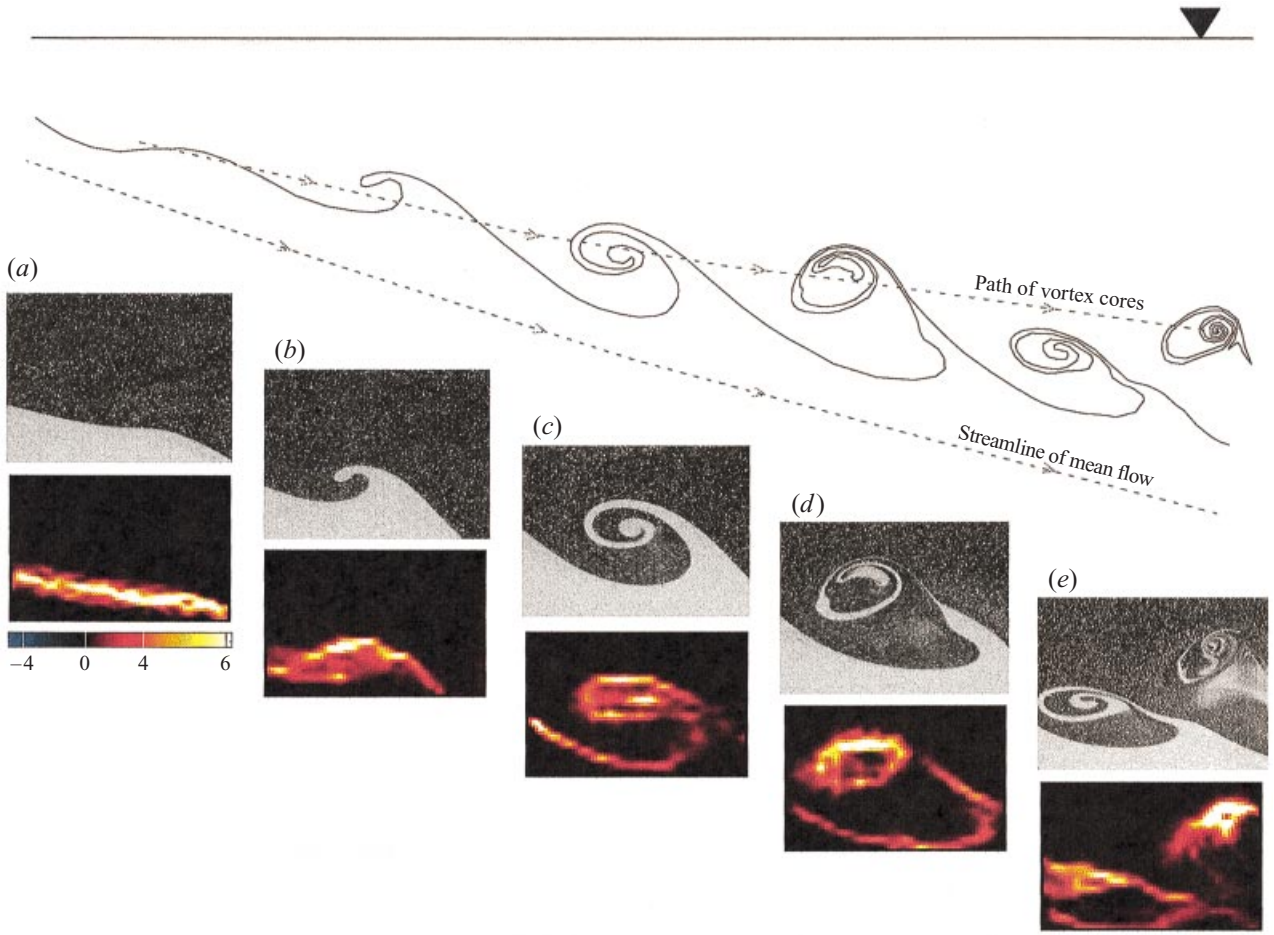


FIGURE 20. Cartoon of modified vortex mechanism.

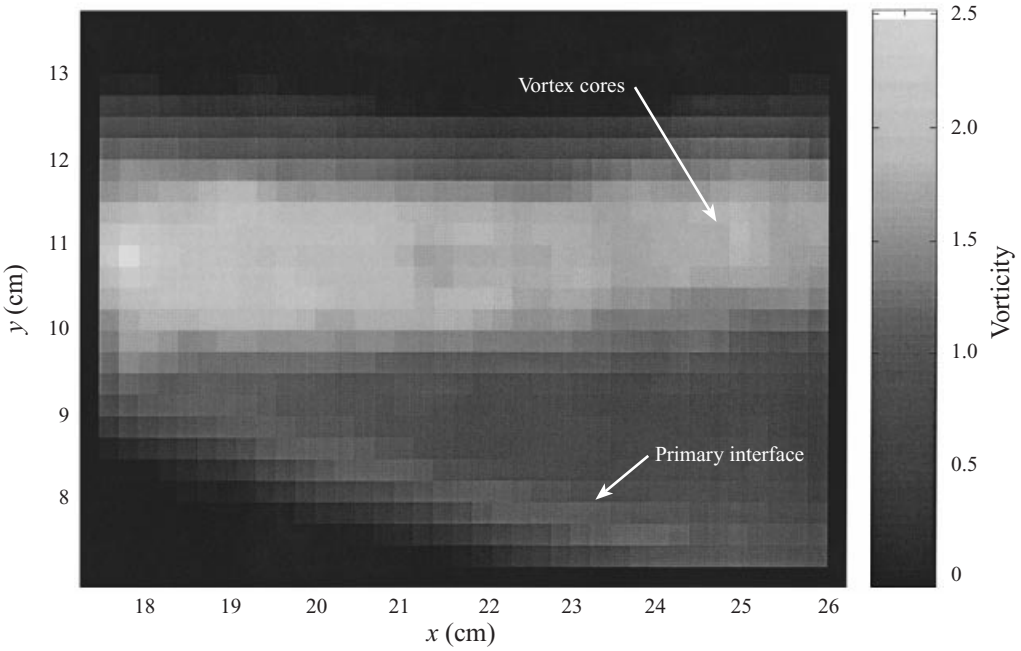


FIGURE 21. Time average of vorticity at pinching off of vortex core.

slower rate than the accelerating dense layer, resulting in a more horizontal trajectory. This process accentuates the separation of the core region from the interface. The subsequent vertical displacement leads to an increase in the separation of the core from the vorticity source as is illustrated by the path lines in figure 20 and is evidenced in frame (*d*). Low-momentum, lighter fluid is drawn into the structure and as the acceleration continues, the core moves away from the interface until it completely pinches off, carrying with it a large portion of the available vorticity. The interface, still inclined, continues to produce new vorticity.

A time-averaged greyscale image of vorticity is presented in figure 21, corresponding to the point of vortex separation seen in figure 20(*d*). The image, obtained by averaging over 52 s (about 18 events), illustrates the horizontal track of the vorticity-containing cores. The weaker track below correlates with the primary interface, plunging at a steeper angle. The velocity field induced by the separating core continues to drive new vorticity along the interface towards the root of its trailing braid, where the secondary core seen in figure 20(*d*) begins to develop. The new core is a weak centre of vorticity since the bulk of the existing vorticity has been removed in the separated core.

The subharmonic component, which results in vortex pairing in the standard shear layer, remains significant but the pairing process is altered. The separation of the first vortex in the subharmonic pair is accentuated by the subharmonic motion while the detachment of the second vortex is hindered. The subharmonic interaction is then between three vorticity structures: the two separated cores and the weaker secondary core of the second structure. Vortices occasionally exhibit a variation in the subharmonic interaction in which a highly separated vortex cannot completely pair with the following structure. A portion of vorticity-containing fluid from the first core is then torn away and remains in the low-momentum stream to interact with the following subharmonic pair.

https://doi.org/10.1017/S002211209800250X Published online by Cambridge University Press

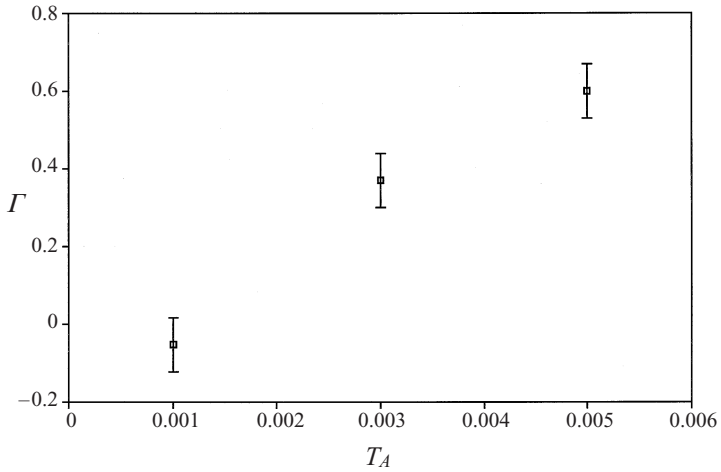


FIGURE 22. Asymmetry factor, Γ, vs. acceleration parameter, T_A. Error bars indicate confidence in measurement.

The argument for the persistence of the mechanisms described by the cartoon in figure 20 into more fully developed regions depends on the continuation of the acceleration as well as on the existence of a region of high density gradient where vorticity can continue to be locally produced. The averaged density profiles in figure 15 show evidence of such a region near the high-momentum stream. The existence of this region can be expected considering our cartoon of the vortex mechanics. The tearing off of vortex cores acts to remove the structure responsible for local stirring (the core) from the immediate vicinity of the interface. The shed cores then transport vorticity and fluid to be mixed away from the interface at which a local maximum in the gradient can persist.

A quantitative measure of the differences in the density profiles shown in figure 15 can be expressed in terms of an asymmetry factor, which we will define as

$$\Gamma = \frac{1}{\theta_\rho \Delta\rho}\int_0^{y_0}(\rho(y)-\rho_1)\mathrm{d}(y-y_{50}) + \frac{1}{\theta_\rho \Delta\rho}\int_{-y_0}^{0}(\rho_2-\rho(y))\mathrm{d}(y-y_{50}), \qquad (5.1)$$

where y_{50} is the location at which the time-averaged density is equal to the average of the two streams, and θ_ρ is the integral density thickness. The asymmetry factor, Γ, is simply the integral of the deviation of the profile from a step centred at y_{50}. A positive value for Γ indicates a bias of the density profile into the low-momentum stream and vice versa. Values of Γ for the profiles in figure 15 are plotted in figure 22 as a function of T_A. The points were chosen from data at roughly equivalent streamwise locations referenced from the point of initial instability, i.e. considering the point of initial instability given in table 1, $x = 32.0$ for $T_A = 0.0012$ is comparable to $x = 32.0$ for $T_A = 0.003$ and $x = 40.0$ for $T_A = 0.0046$. The data show that there is an increase in the bias of the mixing into the lower velocity stream with an increase in the acceleration parameter, T_A.

A second measure of the strength of the mechanism is shown in figure 23. The plot indicates the relative mean concentration of the fluid within the mixed layer, defining the mixed layer boundaries by the 15% and 85% concentration interfaces, y_{15} and

https://doi.org/10.1017/S002211209800250X Published online by Cambridge University Press

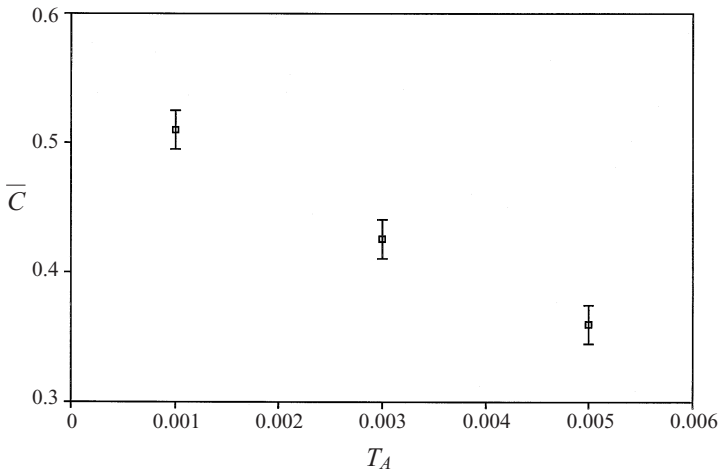


FIGURE 23. Mean concentration, $\bar{C}$, within mixed layer vs. acceleration parameter, T_A. The mixed layer is defined by the 15% and 85% concentration interfaces. Error bars indicate confidence in measurement.

y_{85}, such that

$$\bar{C} = \frac{1}{\delta_{15-85}} \int_{y=y_{85}}^{y=y_{15}} \frac{\rho(y) - \rho_1}{\Delta\rho} \mathrm{d}y \tag{5.2}$$

with $\delta_{15-85} = y_{15} - y_{85}$, for the profiles shown in figure 15. The decrease in $\bar{C}$ with increasing T_A reflects the selective entrainment of fluid from the low-momentum stream as the acceleration increases and the resulting separation of the vortex cores from the interface becomes more pronounced. This is well illustrated in the sequences in figures 9 and 10, in which the large region of low-momentum fluid entrained beneath the separating core is evident.

As we have mentioned in § 3.1, it is the integral of T_A that is responsible for determining the characteristics of the momentum and density profiles. We have used a representative value for T_A, due to limitations in available measurements, to illustrate the effect of its variation on mixed layer development.

The scale over which changes in velocity are relevant to the vortex phenomena discussed is given by the scale over which instabilities develop. This dynamical description of the mechanism agrees with our choice of T_A (see § 1.4) as the relevant parameter. For flows which accelerate gradually over a distance much larger than the scale of instabilities ($T_A \to 0$), the traditional description of a stratified shear layer will apply. For rapidly accelerating flows in which velocity changes are large relative to the wavelength of instabilities ($T_A \uparrow$),the analysis of accelerated shear layers will be relevant.

The observed vortex mechanism has been described as a result of the combined effects of spatial acceleration and buoyancy. It may seem paradoxical then that buoyancy does not appear explicitly in the acceleration parameter. It is implicit, however, in the acceleration term. The effect of buoyancy on the dynamics of the mixing layer is related to the angle of the interface, that is, the separation of the vortices from the interface is proportional to the non-orthogonality of the buoyancy and the velocity vectors. The local acceleration of the flow, in turn, is determined primarily by the baroclinic generation of vorticity along the inclined interface for flows in which $F^2 \sim O(1)$. The buoyancy effects and the acceleration are then both

https://doi.org/10.1017/S002211209800250X Published online by Cambridge University Press

determined through the inclination of the interface. In the Appendix we discuss the relative importance baroclinic generation of vorticity versus production due to cross-stream stretching. The baroclinic production is found to dominate for weakly supercritical flows.

For the lower acceleration case ($T_A = 0.0012$), then, buoyancy is less effective in separating the vortex vertically from the interface as a result of the reduction in interface angle. Furthermore, over the time scale of the instability growth, the acceleration is not significant enough to generate the rapid horizontal separation of the core from its downstream braid that is observed for $T_A = 0.003$ and $T_A = 0.0046$.

At higher values of the acceleration parameter, the acceleration rapidly produces a horizontal separation in the structure and the secondary core becomes more highly developed. In addition, the acceleration maintains a low Richardson number eliminating much of the baroclinic production of opposite-sign vorticity which eventually stops the growth of the mixed layer for unaccelerated flows.

In a simplified manner, we can cartoon the development by considering the upper limit of the interface to extend nearly horizontally from the initial point of instability, and the lower limit bounded by the prediction of the interface location from hydraulic theory. The effect of the vortex mechanism observed then is an increase in the vertical extent of the density layer as the interface angle increases.

6. Summary and conclusions

An experimental and analytical study of a stratified shear layer subjected to a spatial acceleration has revealed the existence of a new finite-amplitude vortex mechanism. Flow visualization and particle imaging velocimetry have been used to identify the primary factors in the mechanics to be the spatial acceleration combined with the effects of buoyancy. The net result of these factors is the separation and pinching off of the developing vortex core from the vorticity source at the interface. In addition to PIV measurements and flow visualizations, laser induced fluorescence (LIF) was used to measure average density fields downstream of the altered vortex pairing region and a significant asymmetry is observed in the structure of the mixing layer, in which a low-gradient region extends into the lower momentum stream. It is proposed that the observed vortex mechanics serve as an instrument for the transfer of vorticity and mass into the slower stream away from the interface and the source of baroclinic production.

These experiments have served to further illustrate the discrepancies between spatial and temporal flow. Examination of flow visualization from Thorpe's temporally accelerating tilting tube experiments (Thorpe 1971, 1973) shows no evidence of the mechanism documented herein. This is expected, however, with the cartoon we have presented in § 5. In the temporally accelerating case, the effect of buoyancy is opposite to that in the spatial case. If we consider one of two equally unstable, offset temporal modes to develop, the effect of a variation in density within the developing structure is to force the offset vortex towards the interface and prevent its separation. In addition, since both layers are accelerating, the convective speed of the instability will accelerate as well, eliminating the mechanism for the horizontal separation of the core from its braids.

We can consider, now, the effect of introducing an expansion in area on a traditional stratified splitter plate experiment such as that detailed in Koop & Browand (1979). From hydraulic theory we know that this will result in a thinning of the faster moving stream (if the flow is supercritical). For geometries involving only a variation

https://doi.org/10.1017/S002211209800250X Published online by Cambridge University Press

in depth, or for variation in width and weak supercritical flow, vorticity generation will be primarily baroclinic and the mechanics we have observed can be expected to play an important role. For strong supercritical flow, cross-stream vortex stretching dominates the production of vorticity. As F^2 increases then, we can expect intervortex interactions to play a more significant role since the vorticity within the developing core intensifies without relying on the baroclinic production at the interface.

In this laboratory experiment the velocity profile is established via surface tension and viscous diffusion. In a stratified geophysical flow, the velocity profile would more likely be a function of the density profile and continuously stratified hydraulics. Nonetheless, many geophysical scenarios can be approximated by two homogeneous layers and this cartoon of the accelerating stratified shear layer will apply. Furthermore, the description is representative of low Richardson number mixing over a large range of barotropic flow for moderate Froude numbers.

This type of mechanism can be expected to be important in other flows in which a spatial acceleration is combined with a transverse component of buoyancy. Besides hydraulically controlled atmospheric and oceanic flows, these features are present in buoyant jets and plumes, particularly those in which the axis is at an angle from the vertical.

Our study of the inclined mixing layer has revealed markedly different vortex dynamics along with significantly modified density structure. These results call into question the applicability of generic ideas of shear-induced mixing to specific mixing problems. In more complex geophysical scenarios involving varied geometries and stratified environments further differences can be expected.

The work presented here is the result of the first author's PhD thesis (Pawlak 1997). Funding was provided by the National Science Foundation and the Office of Naval Research. We would like to thank Professors Juan Lasheras and Ken Melville for making their experimental equipment available to us. We would also like to acknowledge the technical assistance of Dr Jochen Klinke in collecting and processing many of the image sequences. We are grateful to Professor Lasheras and Professor David Farmer for many insightful discussions and comments during the course of our study.

Appendix. Baroclinic vorticity production

For the two-layer wedge flow through a contraction, vorticity is produced by two mechanisms: vortex stretching, resulting from the variation in width of the channel, and baroclinic generation, as a consequence of the inclination of the interface. The relative contributions of each can be estimated by dimensional analysis of the vorticity equation.

$$\frac{\mathrm{D}\boldsymbol{\omega}}{\mathrm{D}t} = \boldsymbol{\omega}\cdot\nabla\boldsymbol{v} + \nu\nabla^2\boldsymbol{\omega} + \frac{\nabla\rho\times\nabla p}{\rho^2}. \tag{A 1}$$

The z-component of the stretching term is given by

$$(\boldsymbol{\omega}\cdot\nabla\boldsymbol{v})_z = \omega_z\left(\frac{\partial u}{\partial z} + \frac{\partial v}{\partial z} + \frac{\partial w}{\partial z}\right). \tag{A 2}$$

If we assume there is no cross-stream variation in u and v, this reduces to

$$(\boldsymbol{\omega}\cdot\nabla\boldsymbol{v})_z = \omega_z\frac{\partial w}{\partial z}. \tag{A 3}$$

https://doi.org/10.1017/S002211209800250X Published online by Cambridge University Press

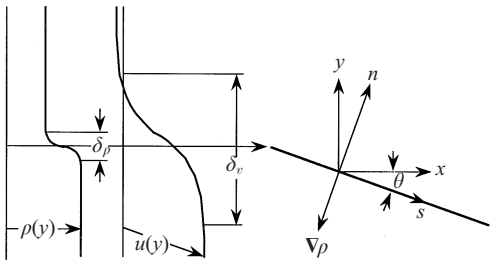


FIGURE 24. Geometry of density gradient vector.

The boundary conditions on the transverse velocity, w, are

$$\left.\begin{aligned} w = \pm\frac{u}{2}\frac{\mathrm{d}b}{\mathrm{d}x}, \quad z = \pm b/2, \\ w = 0, \quad z = 0 \end{aligned}\right\} \tag{A 4}$$

from the tangential velocity condition at the wall for a symmetric channel. The channel width is given by b. Assuming further, that the gradients of u and v do not vary with z, the continuity equation requires that

$$w = C(x, y)z. \tag{A 5}$$

C is then determined from the boundary conditions, (A 4), such that

$$\frac{\partial w}{\partial z} = \frac{u}{b}\frac{\mathrm{d}b}{\mathrm{d}x}. \tag{A 6}$$

From the definition of the z-component of the vorticity,

$$\omega_z = \frac{\partial u}{\partial y} \sim \frac{\Delta u}{\delta_v} = \frac{u}{\delta_v}, \tag{A 7}$$

where δ_v is a shear layer vorticity thickness, and the velocity step, Δu, has been replaced by u, since we have one stagnant layer. The contribution of $-\partial v/\partial x$ has been neglected, which is appropriate if the interface slope, $\mathrm{d}y/\mathrm{d}x$, is not large. Using equations (A 6) and (A 7), the production of z-vorticity by vortex stretching can then be scaled as

$$(\boldsymbol{\omega}\cdot\nabla\boldsymbol{v})_z \simeq \frac{2u^2}{\delta_v b}\frac{\mathrm{d}b}{\mathrm{d}x}. \tag{A 8}$$

The baroclinic generation of z-vorticity is given by

$$\left(\frac{\nabla\rho\times\nabla p}{\rho^2}\right)_z = \frac{1}{\rho^2}\left(\frac{\partial\rho}{\partial x}\frac{\partial p}{\partial y} - \frac{\partial\rho}{\partial y}\frac{\partial p}{\partial x}\right). \tag{A 9}$$

We assume now, that the horizontal pressure gradient is negligible and use the Boussinesq approximation of small variation in density to obtain

$$\left(\frac{\nabla\rho\times\nabla p}{\rho^2}\right)_z = \frac{g}{\bar{\rho}}\frac{\partial\rho}{\partial x}. \tag{A 10}$$

From the flow geometry (figure 24), we can deduce

$$\frac{\partial\rho}{\partial x} = \frac{\partial\rho}{\partial n}\frac{\Delta y}{\Delta s} = \frac{\partial\rho}{\partial n}\sin\theta. \tag{A 11}$$

https://doi.org/10.1017/S002211209800250X Published online by Cambridge University Press

The density gradient can be scaled as

$$\frac{\partial \rho}{\partial n} \sim \frac{\Delta \rho}{\delta_\rho}, \tag{A 12}$$

where δ_ρ is a measure of the density interface thickness. Using equations (A 11) and (A 12), in equation (A 10) and assuming that the angle, θ, is small so that $\sin\theta \simeq \theta \simeq \mathrm{d}y/\mathrm{d}x$, we find

$$\left(\frac{\nabla\rho \times \nabla p}{\rho^2}\right)_z = \frac{g'}{\delta_\rho}\frac{\mathrm{d}y}{\mathrm{d}x}. \tag{A 13}$$

If we now assume that the vorticity and density gradients are constant across the interfaces then integrating equations (A 8) and (A 13) to obtain the total vorticity produced at a given x-location, amounts to multiplying by δ_v and δ_ρ, respectively.

We define the ratio of baroclinic production to vortex stretching production as

$$B_\omega = \frac{\left|\delta_\rho \left(\dfrac{\nabla\rho \times \nabla p}{\rho^2}\right)_z\right|}{|\delta_v\,(\boldsymbol{\omega}\cdot\nabla\boldsymbol{v})_z|}. \tag{A 14}$$

Substituting equations (A 8) and (A 13) into equation (A 14) and rearranging, we find

$$B_\omega = \left|\left[\frac{g'y}{u^2}\right]\left[\frac{(1/y)(\mathrm{d}y/\mathrm{d}x)}{(1/b)(\mathrm{d}b/\mathrm{d}x)}\right]\right|. \tag{A 15}$$

We recognize the first term in (A 15) as the single layer Froude number, $F^2 = u^2/g'y$, where y is the layer depth.

Using two-layer hydraulic theory for the case of strong barotropic flow (see Pawlak & Armi 1997), generalizing to allow for variation of depth and width, we find

$$\frac{1}{y}\frac{\mathrm{d}y}{\mathrm{d}x} = \left[\frac{F^2}{b}\frac{\mathrm{d}b}{\mathrm{d}x} - \frac{1}{y}\frac{\mathrm{d}h}{\mathrm{d}x}\right] \tag{A 16}$$

where h is the total channel depth. Substituting into equation (A 15),

$$B_\omega = \left|\frac{1}{1-F^2}\left[1 - \frac{b}{yF^2}\frac{\mathrm{d}h/\mathrm{d}x}{\mathrm{d}b/\mathrm{d}x}\right]\right|. \tag{A 17}$$

For channel geometries involving no variation in width, there will clearly be no stretching component and we will have $B_\omega = \infty$ with vorticity production being purely baroclinic. For geometries with no variation in depth, equation (A 17) reduces to

$$B_\omega = \left|\frac{1}{1-F^2}\right|. \tag{A 18}$$

Thus for subcritical and weakly supercritical flow ($F^2 < 2$) vorticity production will be primarily due to baroclinicity. For a general channel geometry, involving changes in depth and width, the bracketed term in equation (A 17) will play a more significant role, particularly for shallow flows ($y \ll b$); however, it is clear that for highly supercritical flows, vorticity generation will be dominated by vortex stretching.

https://doi.org/10.1017/S002211209800250X Published online by Cambridge University Press

REFERENCES

Armi, L. 1986 The hydraulics of two flowing layers with different densities. *J. Fluid Mech.* **163**, 27–58.

Armi, L. & Farmer, D. M. 1986 Maximal two-layer exchange through a contraction with barotropic net flow. *J. Fluid Mech.* **164**, 27–58.

Armi, L. & Farmer, D. M. 1988 The flow of Mediterranean water through the Strait of Gibraltar. *Prog. Oceanogr.* **21**, 1–105.

Bernal, L. P. & Roshko, A. 1986 Streamwise vortex structure in plane mixing layers. *J. Fluid Mech.* **170**, 499–525.

Brown, G. L. & Roshko, A. 1974 On density effects and large structure in turbulent mixing layers. *J. Fluid Mech.* **64**, 775–816.

Corcos, G. M. 1988 The role of cartoons in turbulence. In *Perspectives in Fluid Mechanics: Proceedings of a Symposium held on the Occasion of the 70th birthday of Hans Wolfgang Liepmann, Pasadena, California, 10-12 January, 1985*. Lecture Notes in Physics, vol. 320, pp. 48–65. Springer.

Corcos, G. M. & Sherman, F. S. 1976 Vorticity concentration and the dynamics of unstable free shear layers. *J. Fluid Mech.* **73**, 241–264.

Corcos, G. M. & Sherman, F. S. 1984 The mixing layer: deterministic models of a turbulent flow. Part 1. Introduction and the two-dimensional flow. *J. Fluid Mech.* **139**, 29–65.

Farmer, D. M. & Armi, L. 1998 The establishment of stratified flows over topography by small scale entrainment and mixing. *Phil. Trans. R. Soc. Lond.* (in press).

Farmer, D. M. & Freeland, H. 1983 The physical oceanography of fjords. *Prog. Oceanogr.* **12**, 147–219.

Farmer, D. M. & Smith, J. D. 1980 Tidal interaction of stratified flow with a sill in Knight Inlet. *Deap-Sea Res.* **27A**, 239–254.

Fincham, A. & Spedding, G. 1997 Low cost, high resolution DPIV for measurement of turbulent fluid flow. *Exps. Fluids* **23**, 449–462.

Geyer, W. R. & Smith, J. D. 1987 Shear instability in a highly stratified estuary. *J. Phys. Oceanogr.* **17**, 1668–1679.

Goldstein, S. 1931 On the stability of superposed streams of fluids of different densities. *Proc. R. Soc. Lond.* A **132**, 524–548.

Hazel, P. 1972 Numerical studies of the stability of inviscid stratified shear flows. *J. Fluid Mech.* **51**, 39–61.

Hermanson, J. & Dimotakis, P. 1989 Effects of heat release in a turbulent, reacting shear layer. *J. Fluid Mech.* **199**, 333–375.

Holmboe, J. 1962 On the behavior of symmetric waves in stratified shear layers. *Geofys. Publ.* **24**, 67.

Klemp, J. B. & Lilly, D. K. 1975 Dynamics of wave-induced downslope winds. *J. Atmos. Sci.* **32**, 320–339.

Koop, C. G. & Browand, F. K. 1979 Instability and turbulence in a stratified fluid with shear. *J. Fluid Mech.* **93**, 135–159.

Lasheras, J. C., Cho, J. S. & Maxworthy, T. 1986 On the origin and evolution of streamwise vortical structures in a plane, free shear layer. *J. Fluid Mech.* **172**, 231–258.

Lawrence, G. A. 1990 On the hydraulics of Boussinesq and non-Boussinesq two-layer flows. *J. Fluid Mech.* **215**, 457–480.

Lawrence, G. A., Browand, F. & Redekopp, L. 1991 The stability of a sheared density interface. *Phys. Fluids* A **3**, 2360–2370.

Lawrence, G. A., Lasheras, J. C. & Browand, F. K. 1987 Shear instabilities in stratified flow. In *Stratified Flows, Proc. Third Intl Symp. on Stratified Flows* (ed. E. J. List & G. H. Jirka), p. 15. ASCE.

Lemoine, F., Wolff, M. & Lebouche, M. 1996 Simultaneous concentration and velocity measurements using combined laser-induced flourescence and laser Doppler velocimetry: Application to turbulent transport. *Exps. Fluids* **20**, 319–327.

Michalke, A. 1965 On spatially growing disturbances in an inviscid shear layer. *J. Fluid Mech.* **23**, 521–544.

https://doi.org/10.1017/S002211209800250X Published online by Cambridge University Press

Pawlak, G. 1997 Hydraulics, mixing and stability of a two-layer arrested wedge flow. PhD thesis University of California, San Diego.

Pawlak, G. & Armi, L. 1996 Stability and mixing of a two layer exchange flow. *Dyn. Atmos. Oceans* **24**, 139–151.

Pawlak, G. & Armi, L. 1997 Hydraulics of a two-layer arrested wedge flow. *J. Hydr. Res.* **35**, 603–618.

Smith, R. B. 1979 The influence of mountains on the atmosphere *Adv. Geophys.* **21**, 87–230.

Taylor, G. 1931 Effect if variation in density on the stability of superposed streams of fluid. *Proc. R. Soc. Lond.* A **132**, 499–523.

Thorpe, S. 1968 A method of producing a shear flow in a stratified fluid. *J. Fluid Mech.* **32**, 693–704.

Thorpe, S. 1971 Experiments on the instability of stratified shear flows: miscible fluids. *J. Fluid Mech.* **46**, 299–319.

Thorpe, S. 1973 Experiments on instability and turbulence in a stratified shear flow. *J. Fluid Mech.* **61**, 731–751.

Thorpe, S. 1985 Laboratory observations of secondary structures in Kelvin-Helmoltz billows and consequences for ocean mixing. *Geophys. Astrophys. Fluid Dyn.* **34**, 175–199.

Winant, C. D. & Browand, F. K. 1974 Vortex pairing: the mechanism of turbulent mixing-layer growth at moderate reynolds number. *J. Fluid Mech.* **63**, 237–255.

Yonemitsu, N., Swaters, G., Rajaratnam, N. & Lawrence, G. A. 1996 Shear instabilities in arrested salt-wedge flows. *Dyn. Atmos. Oceans* **24**, 173–182.

https://doi.org/10.1017/S002211209800250X Published online by Cambridge University Press